Search for Heavy, Long-Lived Neutralinos that Decay to Photons at CDF II Using Photon Timing

T. Aaltonen,[24] J. Adelman,[14] T. Akimoto,[56] M.G. Albrow,[18] B. Álvarez González,[12] S. Amerio[u],[44] D. Amidei,[35] A. Anastassov,[39] A. Annovi,[20] J. Antos,[15] G. Apollinari,[18] A. Apresyan,[49] T. Arisawa,[58] A. Artikov,[16] W. Ashmanskas,[18] A. Attal,[4] A. Aurisano,[54] F. Azfar,[43] P. Azzurri[s],[47] W. Badgett,[18] A. Barbaro-Galtieri,[29] V.E. Barnes,[49] B.A. Barnett,[26] V. Bartsch,[31] G. Bauer,[33] P.-H. Beauchemin,[34] F. Bedeschi,[47] P. Bednar,[15] D. Beecher,[31] S. Behari,[26] G. Bellettini[q],[47] J. Bellinger,[60] D. Benjamin,[17] A. Beretvas,[18] J. Beringer,[29] A. Bhatti,[51] M. Binkley,[18] D. Bisello[u],[44] I. Bizjak,[31] R.E. Blair,[2] C. Blocker,[7] B. Blumenfeld,[26] A. Bocci,[17] A. Bodek,[50] V. Boisvert,[50] G. Bolla,[49] D. Bortoletto,[49] J. Boudreau,[48] A. Boveia,[11] B. Brau,[11] A. Bridgeman,[25] L. Brigliadori,[44] C. Bromberg,[36] E. Brubaker,[14] J. Budagov,[16] H.S. Budd,[50] S. Budd,[25] K. Burkett,[18] G. Busetto[u],[44] P. Bussey[x],[22] A. Buzatu,[34] K. L. Byrum,[2] S. Cabrera[p],[17] C. Calancha,[32] M. Campanelli,[36] M. Campbell,[35] F. Canelli,[18] A. Canepa,[46] D. Carlsmith,[60] R. Carosi,[47] S. Carrillo[j],[19] S. Carron,[34] B. Casal,[12] M. Casarsa,[18] A. Castro[t],[6] P. Catastini[r],[47] D. Cauz[w],[55] V. Cavaliere[r],[47] M. Cavalli-Sforza,[4] A. Cerri,[29] L. Cerrito[n],[31] S.H. Chang,[28] Y.C. Chen,[1] M. Chertok,[8] G. Chiarelli,[47] G. Chlachidze,[18] F. Chlebana,[18] K. Cho,[28] D. Chokheli,[16] J.P. Chou,[23] G. Choudalakis,[33] S.H. Chuang,[53] K. Chung,[13] W.H. Chung,[60] Y.S. Chung,[50] C.I. Ciobanu,[45] M.A. Ciocci[r],[47] A. Clark,[21] D. Clark,[7] G. Compostella,[44] M.E. Convery,[18] J. Conway,[8] K. Copic,[35] M. Cordelli,[20] G. Cortiana[u],[44] D.J. Cox,[8] F. Crescioli[q],[47] C. Cuenca Almenar[p],[8] J. Cuevas[m],[12] R. Culbertson,[18] J.C. Cully,[35] D. Dagenhart,[18] M. Datta,[18] T. Davies,[22] P. de Barbaro,[50] S. De Cecco,[52] A. Deisher,[29] G. De Lorenzo,[4] M. Dell'Orso[q],[47] C. Deluca,[4] L. Demortier,[51] J. Deng,[17] M. Deninno,[6] P.F. Derwent,[18] G.P. di Giovanni,[45] C. Dionisi[v],[52] B. Di Ruzza[w],[55] J.R. Dittmann,[5] M. D'Onofrio,[4] S. Donati[q],[47] P. Dong,[9] J. Donini,[44] T. Dorigo,[44] S. Dube,[53] J. Efron,[40] A. Elagin,[54] R. Erbacher,[8] D. Errede,[25] S. Errede,[25] R. Eusebi,[18] H.C. Fang,[29] S. Farrington,[43] W.T. Fedorko,[14] R.G. Feild,[61] M. Feindt,[27] J.P. Fernandez,[32] C. Ferrazza[s],[47] R. Field,[19] G. Flanagan,[49] R. Forrest,[8] M. Franklin,[23] J.C. Freeman,[18] H. Frisch,[14] I. Furic,[19] M. Gallinaro,[52] J. Galyardt,[13] F. Garberson,[11] J.E. Garcia,[47] A.F. Garfinkel,[49] P. Geffert,[54] K. Genser,[18] H. Gerberich,[25] D. Gerdes,[35] A. Gessler,[27] S. Giagu[v],[52] V. Giakoumopoulou,[3] P. Giannetti,[47] K. Gibson,[48] J.L. Gimmell,[50] C.M. Ginsburg,[18] N. Giokaris,[3] M. Giordani[w],[55] P. Giromini,[20] M. Giunta[q],[47] G. Giurgiu,[26] V. Glagolev,[16] D. Glenzinski,[18] M. Gold,[38] N. Goldschmidt,[19] A. Golossanov,[18] G. Gomez,[12] G. Gomez-Ceballos,[33] M. Goncharov,[54] O. González,[32] I. Gorelov,[38] A.T. Goshaw,[17] K. Goulianos,[51] A. Gresele,[u],[44] S. Grinstein,[23] C. Grosso-Pilcher,[14] R.C. Group,[18] U. Grundler,[25] J. Guimaraes da Costa,[23] Z. Gunay-Unalan,[36] C. Haber,[29] K. Hahn,[33] S.R. Hahn,[18] E. Halkiadakis,[53] B.-Y. Han,[50] J.Y. Han,[50] R. Handler,[60] F. Happacher,[20] K. Hara,[56] D. Hare,[53] M. Hare,[57] S. Harper,[43] R.F. Harr,[59] R.M. Harris,[18] M. Hartz,[48] K. Hatakeyama,[51] J. Hauser,[9] C. Hays,[43] M. Heck,[27] A. Heijboer,[46] B. Heinemann,[29] J. Heinrich,[46] C. Henderson,[33] M. Herndon,[60] J. Heuser,[27] S. Hewamanage,[5] D. Hidas,[17] C.S. Hill[c],[11] D. Hirschbuehl,[27] A. Hocker,[18] S. Hou,[1] M. Houlden,[30] S.-C. Hsu,[10] B.T. Huffman,[43] R.E. Hughes,[40] U. Husemann,[61] J. Huston,[36] J. Incandela,[11] G. Introzzi,[47] M. Iori[v],[52] A. Ivanov,[8] E. James,[18] B. Jayatilaka,[17] E.J. Jeon,[28] M.K. Jha,[6] S. Jindariani,[18] W. Johnson,[8] M. Jones,[49] K.K. Joo,[28] S.Y. Jun,[13] J.E. Jung,[28] T.R. Junk,[18] T. Kamon,[54] D. Kar,[19] P.E. Karchin,[59] Y. Kato,[42] R. Kephart,[18] J. Keung,[46] V. Khotilovich,[54] B. Kilminster,[40] D.H. Kim,[28] H.S. Kim,[28] J.E. Kim,[28] M.J. Kim,[20] S.B. Kim,[28] S.H. Kim,[56] Y.K. Kim,[14] N. Kimura,[56] L. Kirsch,[7] S. Klimenko,[19] B. Knuteson,[33] B.R. Ko,[17] S.A. Koay,[11] K. Kondo,[58] D.J. Kong,[28] J. Konigsberg,[19] A. Korytov,[19] A.V. Kotwal,[17] M. Kreps,[27] J. Kroll,[46] D. Krop,[14] N. Krumnack,[5] M. Kruse,[17] V. Krutelyov,[11] T. Kubo,[56] T. Kuhr,[27] N.P. Kulkarni,[59] M. Kurata,[56] Y. Kusakabe,[58] S. Kwang,[14] A.T. Laasanen,[49] S. Lami,[47] S. Lammel,[18] M. Lancaster,[31] R.L. Lander,[8] K. Lannon,[40] A. Lath,[53] G. Latino[r],[47] I. Lazzizzera[u],[44] T. LeCompte,[2] E. Lee,[54] S.W. Lee[o],[54] S. Leone,[47] J.D. Lewis,[18] C.S. Lin,[29] J. Linacre,[43] M. Lindgren,[18] E. Lipeles,[10] A. Lister,[8] D.O. Litvintsev,[18] C. Liu,[48] T. Liu,[18] N.S. Lockyer,[46] A. Loginov,[61] M. Loreti[u],[44] L. Lovas,[15] R.-S. Lu,[1] D. Lucchesi[u],[44] J. Lueck,[27] C. Luci[v],[52] P. Lujan,[29] P. Lukens,[18] G. Lungu,[51] L. Lyons,[43] J. Lys,[29] R. Lysak,[15] E. Lytken,[49] P. Mack,[27] D. MacQueen,[34] R. Madrak,[18] K. Maeshima,[18] K. Makhoul,[33] T. Maki,[24] P. Maksimovic,[26] S. Malde,[43] S. Malik,[31] G. Manca,[30] A. Manousakis-Katsikakis,[3] F. Margaroli,[49] C. Marino,[27] C.P. Marino,[25] A. Martin,[61] V. Martin[i],[22] M. Martínez,[4] R. Martínez-Ballarín,[32] T. Maruyama,[56] P. Mastrandrea,[52] T. Masubuchi,[56] M.E. Mattson,[59] P. Mazzanti,[6] K.S. McFarland,[50] P. McIntyre,[54] R. McNulty[h],[30] A. Mehta,[30] P. Mehtala,[24] A. Menzione,[47] P. Merkel,[49] C. Mesropian,[51] T. Miao,[18] N. Miladinovic,[7] R. Miller,[36] C. Mills,[23] M. Milnik,[27] A. Mitra,[1] G. Mitselmakher,[19] H. Miyake,[56] N. Moggi,[6] C.S. Moon,[28] R. Moore,[18] M.J. Morello[q],[47] J. Morlok,[27] P. Movilla Fernandez,[18] J. Mülmenstädt,[29] A. Mukherjee,[18] Th. Muller,[27] R. Mumford,[26] P. Murat,[18] M. Mussini[t],[6] J. Nachtman,[18] Y. Nagai,[56] A. Nagano,[56] J. Naganoma,[58]

K. Nakamura,[56] I. Nakano,[41] A. Napier,[57] V. Necula,[17] C. Neu,[46] M.S. Neubauer,[25] J. Nielsen[e],[29] L. Nodulman,[2]
M. Norman,[10] O. Norniella,[25] E. Nurse,[31] L. Oakes,[43] S.H. Oh,[17] Y.D. Oh,[28] I. Oksuzian,[19] T. Okusawa,[42]
R. Orava,[24] K. Osterberg,[24] S. Pagan Griso[u],[44] C. Pagliarone,[47] E. Palencia,[18] V. Papadimitriou,[18]
A. Papaikonomou,[27] A.A. Paramonov,[14] B. Parks,[40] S. Pashapour,[34] R. Patel,[54] J. Patrick,[18] G. Pauletta[w],[55]
M. Paulini,[13] C. Paus,[33] D.E. Pellett,[8] A. Penzo,[55] T.J. Phillips,[17] G. Piacentino,[47] E. Pianori,[46] L. Pinera,[19]
K. Pitts,[25] C. Plager,[9] L. Pondrom,[60] O. Poukhov[*],[16] N. Pounder,[43] F. Prakoshyn,[16] A. Pronko,[18] J. Proudfoot,[2]
F. Ptohos[g],[18] E. Pueschel,[13] G. Punzi[q],[47] J. Pursley,[60] J. Rademacker[c],[43] A. Rahaman,[48] V. Ramakrishnan,[60]
N. Ranjan,[49] I. Redondo,[32] B. Reisert,[18] V. Rekovic,[38] P. Renton,[43] M. Rescigno,[52] S. Richter,[27] F. Rimondi[t],[6]
L. Ristori,[47] A. Robson,[22] T. Rodrigo,[12] T. Rodriguez,[46] E. Rogers,[25] S. Rolli,[57] R. Roser,[18] M. Rossi,[55]
R. Rossin,[11] P. Roy,[34] A. Ruiz,[12] J. Russ,[13] V. Rusu,[18] H. Saarikko,[24] A. Safonov,[54] W.K. Sakumoto,[50] O. Saltó,[4]
L. Santi[w],[55] S. Sarkar[v],[52] L. Sartori,[47] K. Sato,[18] A. Savoy-Navarro,[45] T. Scheidle,[27] P. Schlabach,[18] A. Schmidt,[27]
E.E. Schmidt,[18] M.A. Schmidt,[14] M.P. Schmidt[†],[61] M. Schmitt,[39] T. Schwarz,[8] L. Scodellaro,[12] A.L. Scott,[11]
A. Scribano[r],[47] F. Scuri,[47] A. Sedov,[49] S. Seidel,[38] Y. Seiya,[42] A. Semenov,[16] L. Sexton-Kennedy,[18] A. Sfyrla,[21]
S.Z. Shalhout,[59] T. Shears,[30] P.F. Shepard,[48] D. Sherman,[23] M. Shimojima[l],[56] S. Shiraishi,[14] M. Shochet,[14]
Y. Shon,[60] I. Shreyber,[37] A. Sidoti,[47] P. Sinervo,[34] A. Sisakyan,[16] A.J. Slaughter,[18] J. Slaunwhite,[40] K. Sliwa,[57]
J.R. Smith,[8] F.D. Snider,[18] R. Snihur,[34] A. Soha,[8] S. Somalwar,[53] V. Sorin,[36] J. Spalding,[18] T. Spreitzer,[34]
P. Squillacioti[r],[47] M. Stanitzki,[61] R. St. Denis,[22] B. Stelzer,[9] O. Stelzer-Chilton,[43] D. Stentz,[39] J. Strologas,[38]
D. Stuart,[11] J.S. Suh,[28] A. Sukhanov,[19] I. Suslov,[16] T. Suzuki,[56] A. Taffard[d],[25] R. Takashima,[41] Y. Takeuchi,[56]
R. Tanaka,[41] M. Tecchio,[35] P.K. Teng,[1] K. Terashi,[51] J. Thom[f],[18] A.S. Thompson,[22] G.A. Thompson,[25]
E. Thomson,[46] P. Tipton,[61] V. Tiwari,[13] S. Tkaczyk,[18] D. Toback,[54] S. Tokar,[15] K. Tollefson,[36] T. Tomura,[56]
D. Tonelli,[18] S. Torre,[20] D. Torretta,[18] P. Totaro[w],[55] S. Tourneur,[45] Y. Tu,[46] N. Turini[r],[47] F. Ukegawa,[56]
S. Vallecorsa,[21] N. van Remortel[a],[24] A. Varganov,[35] E. Vataga[s],[47] F. Vázquez[j],[19] G. Velev,[18] C. Vellidis,[3]
V. Veszpremi,[49] M. Vidal,[32] R. Vidal,[18] I. Vila,[12] R. Vilar,[12] T. Vine,[31] M. Vogel,[38] I. Volobouev[o],[29] G. Volpi[q],[47]
F. Würthwein,[10] P. Wagner,[2] R.G. Wagner,[2] R.L. Wagner,[18] J. Wagner-Kuhr,[27] W. Wagner,[27] T. Wakisaka,[42]
R. Wallny,[9] S.M. Wang,[1] A. Warburton,[34] D. Waters,[31] M. Weinberger,[54] W.C. Wester III,[18] B. Whitehouse,[57]
D. Whiteson[d],[46] A.B. Wicklund,[2] E. Wicklund,[18] G. Williams,[34] H.H. Williams,[46] P. Wilson,[18] B.L. Winer,[40]
P. Wittich[f],[18] S. Wolbers,[18] C. Wolfe,[14] T. Wright,[35] X. Wu,[21] S.M. Wynne,[30] A. Yagil,[10] K. Yamamoto,[42]
J. Yamaoka,[53] U.K. Yang[k],[14] Y.C. Yang,[28] W.M. Yao,[29] G.P. Yeh,[18] J. Yoh,[18] K. Yorita,[14] T. Yoshida,[42] G.B. Yu,[50]
I. Yu,[28] S.S. Yu,[18] J.C. Yun,[18] L. Zanello[v],[52] A. Zanetti,[55] I. Zaw,[23] X. Zhang,[25] Y. Zheng[b],[9] and S. Zucchelli[t][6]

(CDF Collaboration[‡])

[1]Institute of Physics, Academia Sinica, Taipei, Taiwan 11529, Republic of China
[2]Argonne National Laboratory, Argonne, Illinois 60439
[3]University of Athens, 157 71 Athens, Greece
[4]Institut de Fisica d'Altes Energies, Universitat Autonoma de Barcelona, E-08193, Bellaterra (Barcelona), Spain
[5]Baylor University, Waco, Texas 76798
[6]Istituto Nazionale di Fisica Nucleare Bologna, [t]University of Bologna, I-40127 Bologna, Italy
[7]Brandeis University, Waltham, Massachusetts 02254
[8]University of California, Davis, Davis, California 95616
[9]University of California, Los Angeles, Los Angeles, California 90024
[10]University of California, San Diego, La Jolla, California 92093
[11]University of California, Santa Barbara, Santa Barbara, California 93106
[12]Instituto de Fisica de Cantabria, CSIC-University of Cantabria, 39005 Santander, Spain
[13]Carnegie Mellon University, Pittsburgh, PA 15213
[14]Enrico Fermi Institute, University of Chicago, Chicago, Illinois 60637
[15]Comenius University, 842 48 Bratislava, Slovakia; Institute of Experimental Physics, 040 01 Kosice, Slovakia
[16]Joint Institute for Nuclear Research, RU-141980 Dubna, Russia
[17]Duke University, Durham, North Carolina 27708
[18]Fermi National Accelerator Laboratory, Batavia, Illinois 60510
[19]University of Florida, Gainesville, Florida 32611
[20]Laboratori Nazionali di Frascati, Istituto Nazionale di Fisica Nucleare, I-00044 Frascati, Italy
[21]University of Geneva, CH-1211 Geneva 4, Switzerland
[22]Glasgow University, Glasgow G12 8QQ, United Kingdom
[23]Harvard University, Cambridge, Massachusetts 02138
[24]Division of High Energy Physics, Department of Physics,
University of Helsinki and Helsinki Institute of Physics, FIN-00014, Helsinki, Finland
[25]University of Illinois, Urbana, Illinois 61801
[26]The Johns Hopkins University, Baltimore, Maryland 21218
[27]Institut für Experimentelle Kernphysik, Universität Karlsruhe, 76128 Karlsruhe, Germany

^{28}Center for High Energy Physics: Kyungpook National University,
Daegu 702-701, Korea; Seoul National University, Seoul 151-742,
Korea; Sungkyunkwan University, Suwon 440-746,
Korea; Korea Institute of Science and Technology Information, Daejeon,
305-806, Korea; Chonnam National University, Gwangju, 500-757, Korea
^{29}Ernest Orlando Lawrence Berkeley National Laboratory, Berkeley, California 94720
^{30}University of Liverpool, Liverpool L69 7ZE, United Kingdom
^{31}University College London, London WC1E 6BT, United Kingdom
^{32}Centro de Investigaciones Energeticas Medioambientales y Tecnologicas, E-28040 Madrid, Spain
^{33}Massachusetts Institute of Technology, Cambridge, Massachusetts 02139
^{34}Institute of Particle Physics: McGill University, Montréal,
Canada H3A 2T8; and University of Toronto, Toronto, Canada M5S 1A7
^{35}University of Michigan, Ann Arbor, Michigan 48109
^{36}Michigan State University, East Lansing, Michigan 48824
^{37}Institution for Theoretical and Experimental Physics, ITEP, Moscow 117259, Russia
^{38}University of New Mexico, Albuquerque, New Mexico 87131
^{39}Northwestern University, Evanston, Illinois 60208
^{40}The Ohio State University, Columbus, Ohio 43210
^{41}Okayama University, Okayama 700-8530, Japan
^{42}Osaka City University, Osaka 588, Japan
^{43}University of Oxford, Oxford OX1 3RH, United Kingdom
^{44}Istituto Nazionale di Fisica Nucleare, Sezione di Padova-Trento, ^{u}University of Padova, I-35131 Padova, Italy
^{45}LPNHE, Universite Pierre et Marie Curie/IN2P3-CNRS, UMR7585, Paris, F-75252 France
^{46}University of Pennsylvania, Philadelphia, Pennsylvania 19104
^{47}Istituto Nazionale di Fisica Nucleare Pisa, ^{q}University of Pisa,
^{r}University of Siena and ^{s}Scuola Normale Superiore, I-56127 Pisa, Italy
^{48}University of Pittsburgh, Pittsburgh, Pennsylvania 15260
^{49}Purdue University, West Lafayette, Indiana 47907
^{50}University of Rochester, Rochester, New York 14627
^{51}The Rockefeller University, New York, New York 10021
^{52}Istituto Nazionale di Fisica Nucleare, Sezione di Roma 1,
^{v}Sapienza Università di Roma, I-00185 Roma, Italy
^{53}Rutgers University, Piscataway, New Jersey 08855
^{54}Texas A&M University, College Station, Texas 77843
^{55}Istituto Nazionale di Fisica Nucleare Trieste/ Udine, ^{w}University of Trieste/ Udine, Italy
^{56}University of Tsukuba, Tsukuba, Ibaraki 305, Japan
^{57}Tufts University, Medford, Massachusetts 02155
^{58}Waseda University, Tokyo 169, Japan
^{59}Wayne State University, Detroit, Michigan 48201
^{60}University of Wisconsin, Madison, Wisconsin 53706
^{61}Yale University, New Haven, Connecticut 06520

We present the results of the first hadron collider search for heavy, long-lived neutralinos that decay via $\widetilde{\chi}^0_1 \to \gamma \widetilde{G}$ in gauge-mediated supersymmetry breaking models. Using an integrated luminosity of 570 ± 34 pb^{-1} of $p\bar{p}$ collisions at $\sqrt{s} = 1.96$ TeV, we select γ+jet+missing transverse energy candidate events based on the arrival time of a high-energy photon at the electromagnetic calorimeter as measured with a timing system that was recently installed on the CDF II detector. We find 2 events, consistent with the background estimate of 1.3 ± 0.7 events. While our search strategy does not rely on model-specific dynamics, we set cross section limits and place the world-best 95% C.L. lower limit on the $\widetilde{\chi}^0_1$ mass of 101 GeV/c^2 at $\tau_{\widetilde{\chi}^0_1} = 5$ ns.

––––––––   ––––––––

*Deceased

†Deceased

‡With visitors from ^{a}Universiteit Antwerpen, B-2610 Antwerp, Belgium, ^{b}Chinese Academy of Sciences, Beijing 100864, China, ^{c}University of Bristol, Bristol BS8 1TL, United Kingdom, ^{d}University of California Irvine, Irvine, CA 92697, ^{e}University of California Santa Cruz, Santa Cruz, CA 95064, ^{f}Cornell University, Ithaca, NY 14853, ^{g}University of Cyprus, Nicosia CY-1678, Cyprus, ^{h}University College Dublin, Dublin 4, Ireland, ^{i}University of Edinburgh, Edinburgh EH9 3JZ, United Kingdom, ^{j}Universidad Iberoamericana, Mexico D.F., Mexico, ^{k}University of Manchester, Manchester M13 9PL, England, ^{l}Nagasaki Institute of Applied Science, Nagasaki, Japan, ^{m}University de Oviedo, E-33007 Oviedo, Spain, ^{n}Queen Mary, University of London, London, E1 4NS, Eng-

I. INTRODUCTION

Models of gauge-mediated supersymmetry (SUSY) breaking (GMSB) [1] are attractive for several reasons. Theoretically they solve the "naturalness problem" [2] and provide a low mass (warm) dark matter candidate [3]. From an experimental standpoint they provide a natural explanation for the observation of an $ee\gamma\gamma\not{E}_T$ [4, 5] candidate event by the CDF experiment during Run I at the Fermilab Tevatron. In particular, the photon (γ) and missing transverse energy ($\not{E}_T$) can be produced by the decay of the lightest neutralino ($\widetilde{\chi}_1^0$) into a photon and a weakly interacting, stable gravitino ($\widetilde{G}$). While much attention has been given to prompt $\widetilde{\chi}_1^0 \to \gamma\widetilde{G}$ decays, versions of the model that take into account cosmological constraints favor a $\widetilde{G}$ with keV/c^2 mass and a $\widetilde{\chi}_1^0$ with a lifetime that is on the order of nanoseconds or more [6].

Here we describe in detail [7] the first search for heavy, long-lived neutralinos using photon timing at a hadron collider in the $\gamma + \text{jet} + \not{E}_T$ final state where we require at least one jet and at least one photon. The data comprise an integrated luminosity of 570 ± 34 pb^{-1} of $p\bar{p}$ collisions at $\sqrt{s} = 1.96$ TeV from the Tevatron collected with the CDF II detector [8]. Previous searches for sub-nanosecond [9, 10] and nanosecond-lifetime [10] $\widetilde{\chi}_1^0 \to \gamma\widetilde{G}$ decays using non-timing techniques have yielded null results. The present results extend the sensitivity to larger $\widetilde{\chi}_1^0$ lifetimes and masses.

The structure of this paper is as follows: the remainder of this section provides a more detailed motivation for the search and describes the CDF detector, in particular the recently installed timing system on the electromagnetic calorimeters (the "EMTiming" system) that is used to measure the time of arrival of photons. Section II describes how photons from heavy, long-lived particles would interact with the detector and how the standard identification criteria for prompt photons are modified to keep the identification efficiency high for delayed photons. The section further describes the photon timing measurement. We describe the data sample in Section III and discuss the event pre-selection criteria. Section IV describes the various background sources as well as the methods of estimating the rate at which they populate the signal region. After a description and estimation of the acceptance for GMSB events in Section V, we continue in Section VI with a description of the optimization procedure and the expected sensitivity. The data are studied in Section VII and limits are set on GMSB with a model-independent discussion of the sensitivity. Section VIII concludes with the final results and a dis-

cussion of the future prospects for a similar analysis with more data.

A. Theory and Phenomenology

Many minimal GMSB models are well specified with a small number of free parameters. The electroweak symmetry breaking mechanism originates in a "hidden sector" (not further specified in the model) and is mediated to the visible scalars and fermions by messenger fields; for more details see [1] and references therein. The free parameters of the minimal GMSB model are as follows: the messenger mass scale, M_m; the number of messenger fields, N_m; a parameter Λ that determines the gaugino and scalar masses; the ratio of the neutral Higgs vacuum expectation values, $\tan(\beta)$; and the sign of the higgsino mass parameter, $\text{sign}(\mu)$. For models with $N_m = 1$ and low $\tan(\beta) \lesssim 30$ the weakly interacting $\widetilde{G}$ is the lightest supersymmetric particle (LSP) and the next-to-lightest supersymmetric particle (NLSP) is the lightest neutralino $\widetilde{\chi}_1^0$. For models with $N_m > 1$ or $\tan(\beta) \gtrsim 30$, the NLSP is a slepton (mostly $\tilde{\tau}_1$) [11]. As there are many GMSB parameter combinations that match this phenomenology, representative "model lines" have been identified that allow a good specification of the model with only one free parameter that sets the particle masses. This analysis follows line 8 of the Snowmass Points and Slopes (SPS 8) proposal [12] and assumes $M_m = 2\Lambda$, $\tan(\beta) = 15$, $\text{sgn}(\mu) = 1$, $N_m = 1$, and R-parity conservation. In this model the $\widetilde{\chi}_1^0$ decays via $\widetilde{\chi}_1^0 \to \gamma\widetilde{G}$ with a branching ratio of $\sim$100% but leaves the $\widetilde{\chi}_1^0$ mass and lifetime as free parameters.

Non-minimal GMSB models with a non-zero $\widetilde{\chi}_1^0$ lifetime and a $\sim$1-1.5 keV/c^2 mass $\widetilde{G}$ are favored as they are consistent with current astronomical observations and models of the early universe that take inflation into account [13]. If the $\widetilde{G}$'s are too light ($\lesssim$1 keV/c^2), they can destroy the nuclei produced during big bang nucleosynthesis, leading to a cosmic microwave background that is different from observations [6]. If they are too heavy ($\gtrsim$1 keV/c^2), while they are a warm dark matter candidate [3] and consistent with models of galaxy structure formation, their density can cause the universe to overclose. To include the proper GMSB messenger particle decays and lifetimes, an additional SUSY breaking scale is included and provides an additional parameter in the model that relates the $\widetilde{\chi}_1^0$ lifetime with the $\widetilde{G}$ and the $\widetilde{\chi}_1^0$ masses. In this formulation [1] our parameter choices, SPS 8, favor a lifetime of several nanoseconds for the 100 GeV/c^2 $\widetilde{\chi}_1^0$ mass range, just above current exclusions [9, 10].

In $p\bar{p}$ collisions supersymmetric particles are pair-produced due to R-parity conservation. We probe a range of Λ not already excluded at 95% confidence level (C.L.) in previous collider experiments [9, 10] where the squarks and gluinos have masses of $\sim$600-800 GeV/c^2

land, ^{o}Texas Tech University, Lubbock, TX 79409, ^{p}IFIC(CSIC-Universitat de Valencia), 46071 Valencia, Spain, ^{x}Royal Society of Edinburgh/Scottish Executive Support Research Fellow,
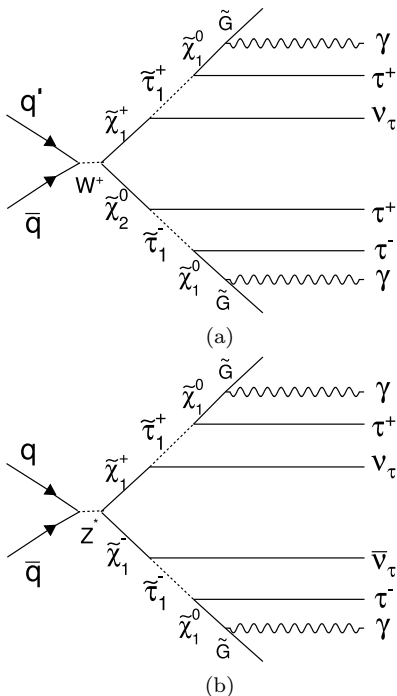
FIG. 1: Feynman diagrams of the dominant tree-production processes at the Fermilab Tevatron for the SPS 8 GMSB model line. The taus and second photons, if available, can be identified as jets in the detector. Note that only one choice for the charge is shown.

and the sleptons and gauginos have masses of ∼100-300 GeV/c^2. At the Tevatron, with $\sqrt{s} = 1.96$ TeV, squarks and gluinos are too heavy to have significant production cross sections, hence gaugino pair-production dominates [1]. Individually, $\widetilde{\chi}_2^0 \widetilde{\chi}_1^{\pm}$ and $\widetilde{\chi}_1^+ \widetilde{\chi}_1^-$ production, as shown in Fig. 1, contribute 45% and 25%, respectively, of the total GMSB production cross section (σ_{prod}). The rest of the production is mostly slepton pairs. We note that σ_{prod} is independent of the $\widetilde{\chi}_1^0$ lifetime.

This analysis focuses on the $\gamma + \not{E}_T$ final state which is expected to be more sensitive to the favored nanosecond lifetime scenario [14]. To identify GMSB events, we use the CDF II detector. As shown in Fig. 1, each gaugino decays (promptly) to a $\widetilde{\chi}_1^0$ in association with taus whose decays can be identified as jets [15]. Whether the $\widetilde{\chi}_1^0 \to \gamma \widetilde{G}$ decay occurs either inside or outside the detector volume depends on the $\widetilde{\chi}_1^0$ decay length (and the detector size). The $\widetilde{\chi}_1^0$'s and/or the $\widetilde{G}$'s leaving the detector give rise to $\not{E}_T$ since they are weakly interacting particles (the neutrinos in the event also affect the $\not{E}_T$). Depending on whether one or two $\widetilde{\chi}_1^0$'s decay inside the detector, the event has the signature of high energy $\gamma\gamma + \not{E}_T$ or $\gamma + \not{E}_T$, often with one or more additional particles from the heavier sparticle decays. These are identifiable as an additional jet(s) in the detector. We do not require the explicit identification of a tau. This has the advantage of reducing the model dependence of our results, making

them applicable to other possible gaugino decay models. A study to see if there is additional sensitivity from adding τ identification to the analysis is in progress.

The arrival time of photons at the detector allows for a good separation between nanosecond-lifetime $\widetilde{\chi}_1^0$'s and promptly produced standard model (SM) photons as well as non-collision backgrounds. Figure 2(a) illustrates a $\widetilde{\chi}_1^0 \to \gamma \widetilde{G}$ decay in the CDF detector after a macroscopic decay length. A suitable timing separation variable is

$$t_{\mathrm{corr}} \equiv (t_f - t_i) - \frac{|\vec{x}_f - \vec{x}_i|}{c}, \qquad (1)$$

where $t_f - t_i$ is the time between the collision t_i and the arrival time t_f of the photon at the calorimeter, and $|\vec{x}_f - \vec{x}_i|$ is the distance between the position where the photon hits the detector and the collision point. Here, t_{corr} is the photon arrival time corrected for the collision time and the time-of-flight. Prompt photons will produce $t_{\mathrm{corr}} \equiv 0$ while photons from long-lived particles will appear "delayed" ($t_{\mathrm{corr}} > 0$), ignoring resolution effects. Figure 2(b) shows the simulated distribution of t_{corr} for a GMSB signal, prompt photons, and non-collision backgrounds in the detector.

B. Overview of the Search

This search selects photons with a delayed arrival time from a sample of events with a high transverse energy (E_T) isolated photon, large $\not{E}_T$, and a high-E_T jet to identify gaugino cascade decays. The background to this search can be separated into two types of sources: collision and non-collision backgrounds. Collision backgrounds come from SM production, such as strong interaction (QCD) and electroweak processes. Non-collision backgrounds come from photon candidates that are either emitted by cosmic ray muons as they traverse the detector or are from beam related backgrounds that produce an energy deposit in the calorimeter that is reconstructed as a photon.

The search was performed as a blind analysis, picking the final selection criteria based on the signal and background expectations alone. The background rates in the signal region are estimated using t_{corr} control regions from the same $\gamma + \mathrm{jet} + \not{E}_T$ data sample and comparing to the distribution shapes of the various backgrounds. A Monte Carlo (MC) simulation is used to model the GMSB event dynamics and timing in the detector and to estimate the signal expectations. Combining these backgrounds and signal event estimates permits a calculation of the most sensitive combination of event requirements. We note that the jet requirement helps make this search sensitive to any model that produces a large mass particle decaying to a similar final state.
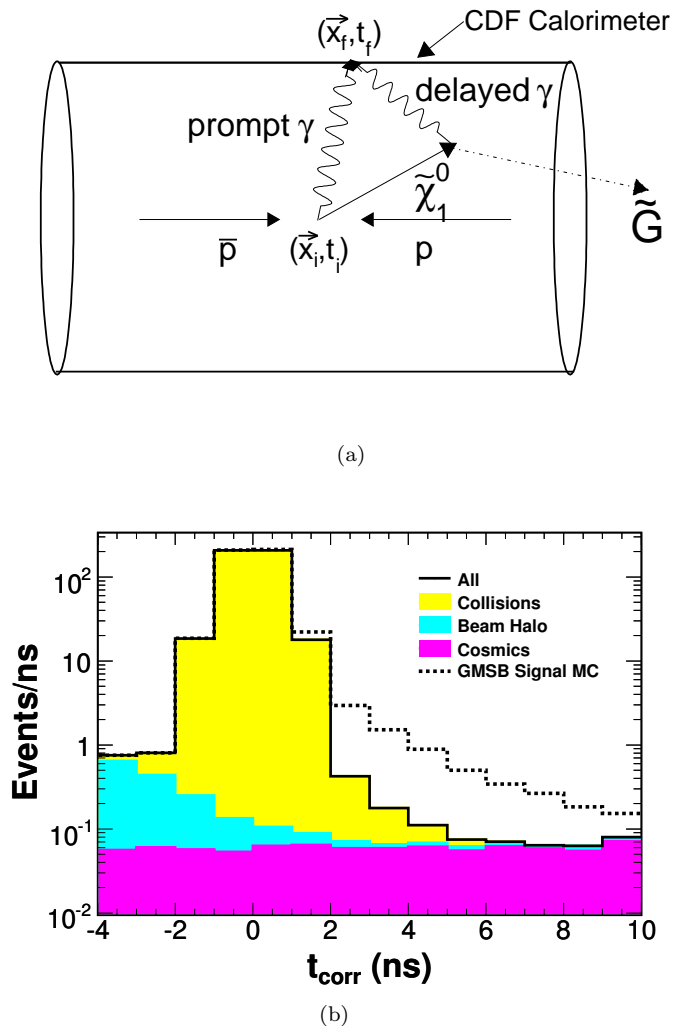
(a)

(b)

FIG. 2: (a) The schematic of a long-lived $\widetilde{\chi}_1^0$ decaying into a $\widetilde{G}$ and a photon inside the detector. While the $\widetilde{G}$ leaves undetected the photon travels to the detector wall and deposits energy in the detector. A prompt photon would travel directly from the collision point to the detector walls. Relative to the expected arrival time, the photon from the $\widetilde{\chi}_1^0$ would appear "delayed." (b) The t_{corr} distribution for a simulated GMSB signal at an example point of $m_{\widetilde{\chi}_1^0} = 100$ GeV/c^2 and $\tau_{\widetilde{\chi}_1^0} = 5$ ns as well as for standard model and non-collision backgrounds.

C. The CDF II Detector and the EMTiming System

The CDF II detector is a general-purpose magnetic spectrometer, whose detailed description can be found in [8] and references therein. The salient components are summarized here. The magnetic spectrometer consists of tracking devices inside a 3-m diameter, 5-m long superconducting solenoid magnet that operates at 1.4 T. A set of silicon microstrip detectors (SVX) and a 3.1-m long drift chamber (COT) with 96 layers of sense wires measure the position ($\vec{x}_i$) and time (t_i) of the $p\bar{p}$ interac-

tion and the momenta of charged particles. Muons from the collision or cosmic rays are identified by a system of drift chambers situated outside the calorimeters in the region with pseudorapidity $|\eta| < 1.1$. The calorimeter consists of projective towers ($\delta\phi = 15°$ and $\delta\eta \approx 0.1$) with electromagnetic and hadronic compartments and is divided into a central barrel that surrounds the solenoid coil ($|\eta| < 1.1$) and a pair of end-plugs that cover the region $1.1 < |\eta| < 3.6$. Both calorimeters are used to identify and measure the energy and position of photons, electrons, jets, and $\not{E}_T$.

The electromagnetic calorimeters were recently instrumented with a new system, the EMTiming system (completed in Fall 2004), which is described in detail in [16] and references therein. The following features are of particular relevance for the present analysis. The system measures the arrival time of electrons and photons in each tower with $|\eta| < 2.1$ using the electronic signal from the EM shower in the calorimeter. In the region $|\eta| < 1.1$, used in this analysis, photomultiplier tubes (PMTs) on opposite azimuthal sides of the calorimeter tower convert the scintillation light generated by the shower into an analog electric signal. The energy measurement integrates the charge over a 132 ns timing window around the collision time from ~20 ns before the collision until ~110 ns afterwards. New electronics inductively branches off ~15% of the energy of the anode signal and sends it to a discriminator. If the signal for a tower is above 2 mV (~3-4 GeV energy deposit), a digital pulse is sent to a time-to-digital converter (TDC) that records the photon arrival time and is read out for each event by the data-acquisition system. The resolution of the time of arrival measurement is 0.50 ± 0.01 ns for the photon energies used in this analysis.

II. PHOTON IDENTIFICATION AND TIMING

The CDF detector has been used for the identification (ID) of high-energy photons for many years, and a standardized set of ID criteria (cuts) for the region $|\eta| < 1.0$ is now well established. Each cut is designed to separate real, promptly produced photons from photons from $\pi^0 \to \gamma\gamma$ decays, hadronic jets, electrons, and other backgrounds, see [7, 9, 17] for more details and the Appendix for a description of the ID variables.

Unlike photons from SM processes, "delayed" photons from long-lived $\widetilde{\chi}_1^0$'s are not expected to hit the calorimeter coming directly from the collision point [14]. As shown in Fig. 2(a), $\widetilde{\chi}_1^0$'s with a long lifetime and small boost can produce a photon from $\widetilde{\chi}_1^0 \to \gamma\widetilde{G}$ with a large path length from the collision position to the calorimeter (large t_{corr}). We define the photon incident angle at the face of the EM calorimeter, ψ, as the angle between the momentum vector of the photon from the $\widetilde{\chi}_1^0$ and the vector to the center of the detector. For convenience we consider the ψ projection onto the (r, z)-plane and label it α, and the ψ projection onto the (r, ϕ)-plane and label
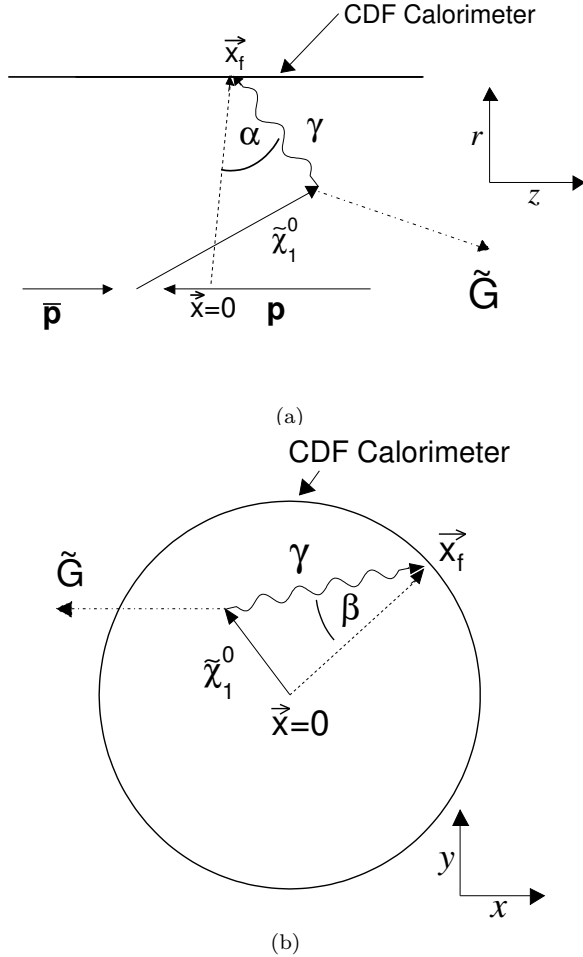
(a)

(b)

FIG. 3: The definitions of the α and β incident angles using schematic diagrams of a long-lived $\widetilde{\chi}_1^0$ decaying to a photon and a $\widetilde{G}$ in the CDF detector. The angles α and β are the projections of the incident angle ψ at the front face of the calorimeter in the (r,z)- and the (r,ϕ)-plane, respectively.
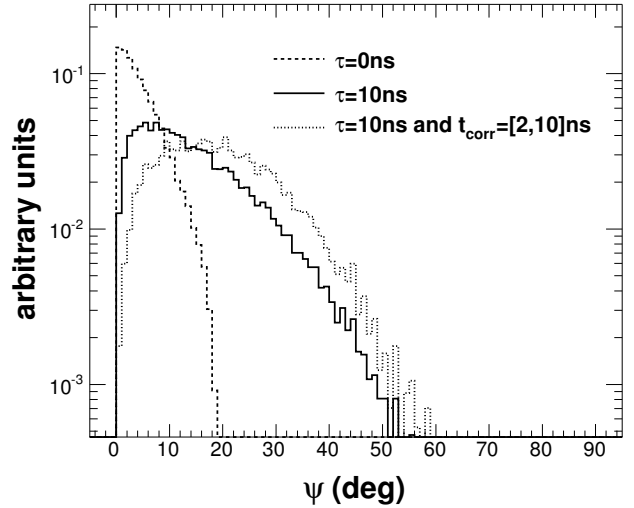

FIG. 4: The distribution of the total incident angle ψ at the front face of the calorimeter for simulated photons from $\widetilde{\chi}_1^0$'s with $m_{\widetilde{\chi}_1^0} = 110$ GeV/c^2. "Prompt" photons from $\widetilde{\chi}_1^0$'s with a lifetime of 0 ns (solid) are compared to photons from $\widetilde{\chi}_1^0$'s with a lifetime 10 ns (dashed). The dotted histogram shows the distribution for a lifetime of 10 ns for photons with $2 \leq t_{\rm corr} \leq 10$ ns and shows that, as expected, delayed photons can have a significant incident angle.

it β; see Fig. 3. This distinction is made as the photon ID variable efficiencies vary differently between α and β.

Figure 4 compares the ψ distribution for prompt, SM-like photons and photons from long-lived $\widetilde{\chi}_1^0$'s. Each are simulated as the decay product of a $\widetilde{\chi}_1^0$ with $m_{\widetilde{\chi}_1^0} = 110$ GeV/c^2 using the PYTHIA MC generator [18]. The distributions of promptly produced photons [19] have a maximum at $\psi=0°$ and extend to $\sim18°$ in α while β is always $\ll 1°$ as the beam has negligible extent in the x-y plane. The most common angle ψ for a simulated neutralino sample with $\tau_{\widetilde{\chi}_1^0} = 10$ ns is $\sim10°$ and extends out to maximum angles of $\sim60°$ and $\sim40°$ in α and β respectively. For this sample, the majority of photons arrive at angles between 0 and 40° total incident angle. The mean of the distribution rises as a function of $\tau_{\widetilde{\chi}_1^0}$ but becomes largely independent of $m_{\widetilde{\chi}_1^0}$ and $\tau_{\widetilde{\chi}_1^0}$ in the range $10 < \tau_{\widetilde{\chi}_1^0} < 35$ ns. Also shown is the distribution for delayed photons, selected with $2 < t_{\rm corr} < 10$ ns, similar to a typical final analysis requirement. The delayed photon requirement shifts the maximum of the distribution of ψ from $\sim10°$ to $\sim25°$. As the incident angles of

photons from long-lived particles are much larger than for prompt photons, the standard selection criteria are re-examined and modified where necessary.

To verify that we can robustly and efficiently identify photons from heavy, long-lived particles, we examine the efficiencies of the photon ID variables as a function of α and β separately. As we will see the standard photon identification requirements are slightly modified for this search; each is listed in Table I. To study photon showers at a wide variety of angles in the calorimeter, we create a number of data and MC samples of photons and electrons. An electron shower in the calorimeter is very similar to that from a photon, but electrons can be selected with high purity. We create two samples of $W \to e\nu$ events, one from data, and the other simulated using the PYTHIA MC generator and the standard, GEANT based, CDF detector simulation [20]. Each must pass the requirements listed in Table II. Similarly, two samples of MC photons are generated using $\widetilde{\chi}_1^0 \to \gamma\widetilde{G}$ decays with $m_{\widetilde{\chi}_1^0} = 110$ GeV/c^2 and $\tau_{\widetilde{\chi}_1^0} = 0$ ns and $\tau_{\widetilde{\chi}_1^0} = 10$ ns respectively to cover the region $0 \leq \psi \leq 60°$. The highest E_T photon in the event is required to be the decay product of a $\widetilde{\chi}_1^0$ and to pass the E_T, η, and fiducial requirements listed in Table I.

Figure 5 compares the distributions of the photon ID variables for the $\tau_{\widetilde{\chi}_1^0} = 0$ and $\tau_{\widetilde{\chi}_1^0} = 10$ ns samples. A visual comparison shows that the differences are, on average, very small. Figure 6 shows the efficiency of the final set of ID requirements for MC photons and electrons from data as a function of incident angles α and β
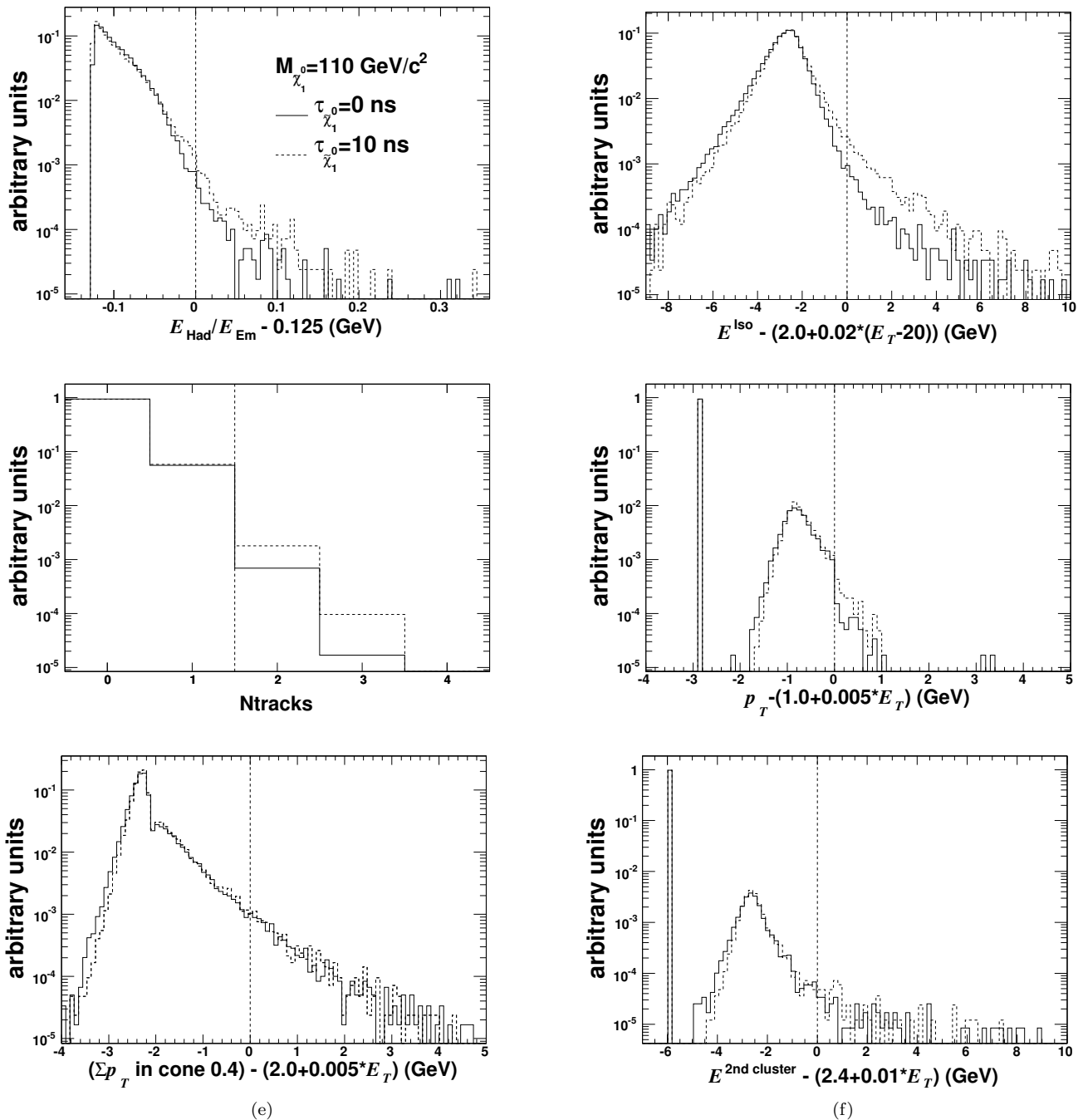
(e)

(f)

FIG. 5: A simulation of the ID variable distributions (minus their requirement value) for photons in a GMSB model with $m_{\widetilde{\chi}_1^0} = 110$ GeV/c^2. The solid line is for prompt photons, simulated as decay photons from $\widetilde{\chi}_1^0$'s with a lifetime of 0 ns and the dashed line is for photons from long-lived $\widetilde{\chi}_1^0$'s with a lifetime of 10 ns. Entries to the left of the dashed vertical line pass the corresponding requirement. The bin at -2.8 in (d) collects the photons that have no track within the isolation cone. In (f) the bin at -6 shows the photons that have no 2nd CES cluster nearby. The distributions for all ID variables do not change significantly between the prompt and the long-lived case except for slight deviations in the energy isolation in (b) as discussed in the text.

(taking the photon position from the measured center of the calorimeter energy cluster). The efficiencies are very similar and constant except at large values of β where the efficiency drops, which is where real collision data are not available. The drop in efficiency at large β is due to the photon shower in the calorimeter traversing into the neighboring tower in ϕ. Because the photons are identified and measured as clusters in the calorime-

ter [17], this decreases the cluster-energy sum while increasing the isolation energy. Therefore, the photon appears non-isolated and the isolation efficiency falls from $\sim 98\%$ at $\beta = 0°$ to $\sim 90\%$ at $\beta = 50°$. This is not a problem for large α as energy leakage into the neighboring tower in η is included in the energy sum. The total photon identification efficiency as a function of ψ in this regime falls from $\sim 93\%$ to $\sim 80\%$. However, since in our

$E_T > 30$ GeV and $|\eta| \leq 1.0$

Fiducial: not near the boundary, in ϕ or z, of a
  calorimeter tower

$E_{\mathrm{Had}}/E_{\mathrm{EM}} < 0.125$

Energy in a $\Delta R = 0.4$ cone around the photon
  excluding the photon energy:
  $E^{\mathrm{Iso}} < 2.0$ GeV $+ 0.02 \cdot (E_T - 20$ GeV$)$

No tracks pointing at the cluster or
  one with $p_T < 1.0$ GeV$/c + 0.005 \cdot E_T$

Σp_T of tracks in a 0.4 cone < 2.0 GeV$/c + 0.005 \cdot E_T$

$E^{\mathrm{2^{nd}cluster}} < 2.4$ GeV $+ 0.01 \cdot E_T$

$\mathrm{A_P} = \frac{|E_{\mathrm{PMT1}} - E_{\mathrm{PMT2}}|}{E_{\mathrm{PMT1}} + E_{\mathrm{PMT2}}} < 0.6$

TABLE I: The photon identification and isolation selection requirements. These are the standard requirements with the $\chi^2_{\mathrm{CES}} < 20$ requirement removed. These variables are described in more detail in [9, 17] and the Appendix.

Electron Requirements
$E_T > 30$ GeV and $|\eta| \leq 1.0$
Fiducial: not near the boundary, in ϕ or z, of a calorimeter tower
$0.9 < E/p < 1.1$ or $p_T > 50$ GeV$/c$
Track traverses ≥ 3 stereo and ≥ 3 axial COT superlayers with 5 hits each
Additional requirements to reject electrons from $\gamma \to ee$
Global Event Requirements
$\not{E}_T > 30$ GeV
Exactly 1 vertex with $N_{\mathrm{trks}} \geq 4$ and $|z| < 60$ cm
Transverse mass of the electron and $\not{E}_T$: $50 < m_T < 120$ GeV$/c^2$

TABLE II: The requirements used to select electrons from $W \to e\nu$ events to validate the ID efficiency of simulated photons. These are topological and global event cuts in combination with loose calorimetry but tight track quality requirements. This produces a sample that contains electrons with high purity but has a low bias for calculating the efficiency of photon ID requirements vs. incident angle. The vertex reconstruction algorithm is described in Section II A and uses tracks passing the requirements listed in Table III. These variables are summarized in the Appendix and described in more detail in [8].

ψ region the fraction of events with large β is small (see Fig. 4), even at large $\tau_{\widetilde{\chi}^0_1}$, the ID criteria are only $\sim 1.5\%$ less efficient for photons for the $\tau_{\widetilde{\chi}^0_1} = 10$ ns sample than for the prompt sample. Thus, the majority of the standard requirements are not changed for the search. The efficiency variation as a function of angle is taken into account by using the detector simulation for the efficiencies and assigning a 5% systematic uncertainty to the overall
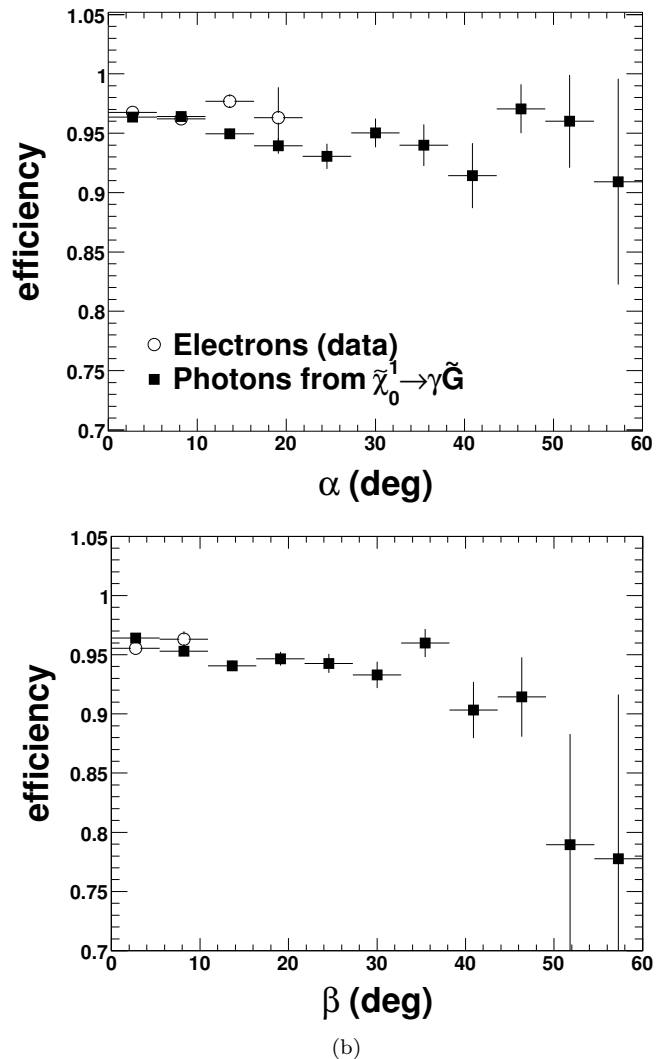

FIG. 6: The efficiencies for photons and electrons to pass the ID requirements in Table I vs. incident angles α and β. The solid squares represent MC photons from $\widetilde{\chi}^0_1 \to \gamma \widetilde{G}$ decays ($m_{\widetilde{\chi}^0_1} = 110$ GeV$/c^2$, $\tau_{\widetilde{\chi}^0_1} = 10$ ns) while the empty circles represent electrons from a $W \to e\nu$ data sample that pass the requirements in Table II. The efficiency falls by $\sim 15\%$ from $0°$ to $60°$ in β. This effect is mostly due to the energy isolation requirement, as discussed in the text.

photon ID efficiency measurement.

The comparison of the photon shower-maximum profile to test-beam expectations, χ^2_{CES} [17], is removed from the photon identification requirements because it becomes inefficient at large angles. The shower for a photon that hits the shower-maximum detector (CES) at a large value of α (β) angle would spread out and have a larger-than-expected RMS in the z (ϕ) direction due to the projection. A GEANT simulation [20] shows the efficiency of the χ^2_{CES} requirement is constant at small angles, but then falls off rapidly at large angles. Thus, the photon χ^2_{CES} requirement is removed.

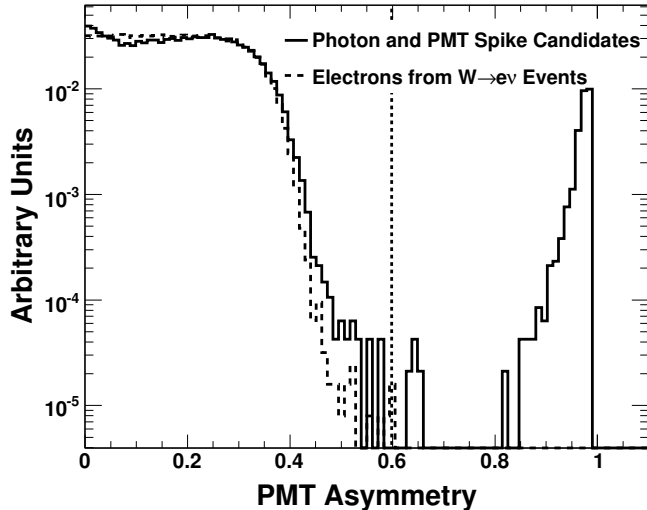A second change to the standard photon ID is to add a requirement to remove high-energy photon candidates

FIG. 7: A comparison of the PMT asymmetry, A_P, for a photon+$\not{E}_T$ sample that contains both PMT spikes and real photons, and a sample of electrons from $W \to e\nu$ events. PMT spikes can be effectively removed by requiring the asymmetry to be less than 0.6.

that are caused by a high-voltage breakdown ("spike") between the PMT photocathode and the surrounding material. Such an occurrence can produce false photon candidates that are uncorrelated with the collision and appear delayed in time. Spikes are identified by the asymmetry of the two energy measurements of the PMTs of a tower:

$$A_P = \frac{|E_{PMT1} - E_{PMT2}|}{E_{PMT1} + E_{PMT2}} \qquad (2)$$

where E_{PMT1} and E_{PMT2} are the two PMT energies. Figure 7 compares photon candidates from both real photons and spikes to real electrons from $W \to e\nu$ events. The photon candidates pass all but the A_P identification requirements shown in Table I in events with $\not{E}_T > 30$ GeV, while the electrons selected pass the requirements in Table IV. As shown in the figure, a requirement of $A_P < 0.6$ rejects $\sim$100% of all spikes with a minimal loss in effeciency for real photons. Thus, this source will be neglected in the background estimate.

A. Measurement of the Collision Time and Position

The corrected photon time is a combination of the measurements of the photon arrival time and position using the EMTiming system and the primary interaction position and time using the COT. We begin with a description of a new vertexing algorithm that provides this time and continue with the EMTiming measurement and the final t_{corr} calculation.

$p_T > 0.3$ GeV/c
$p_T > 1.4$ GeV/c or passes the slow proton rejection cuts if charge> 0
$\|\eta\| < 1.6$
$\|z_0\| < 70$ cm
$Err(z_0) < 1$ cm
$\|t_0\| < 40$ ns
$0.05 < Err(t_0) < 0.8$ ns
Traverses $\geq$3 stereo and $\geq$3 axial COT superlayers with 5 hits each

TABLE III: The set of requirements for tracks to be included in the vertex reconstruction. These are the standard tracking requirements [8], but with additional quality requirements on the t_0 measurement and a slow proton rejection requirement [21] to remove tracks that likely have a mis-measured track t_0. These variables are described in the Appendix.

$E_T > 20$ GeV and $\|\eta\| \leq 1.0$
Fiducial: not near the boundary, in ϕ or z, of a calorimeter tower
$E_{Had}/E_{Em} < 0.055 + 0.00045 \cdot E$
$\chi^2_{Strip} < 10$
$Lshr < 0.2$
$p_T > 10$ GeV/c
$E^{Iso} < 0.1 \cdot E_T$
$-3 < \Delta x \cdot q < 1.5$ and $\|\Delta z\| < 3$ cm
$\|z_0\| < 60$ cm
$p_T > 50$ GeV/c or $0.5 < E/p < 2.0$
Track traverses $\geq$3 stereo and $\geq$3 axial COT superlayers with 5 hits each

TABLE IV: The identification requirements for use in selecting electrons with high purity to study the vertexing performance. Note that "q" is the charge of the electron. The identification requirements are summarized in the Appendix and described in more detail in [8].

The standard vertexing algorithms [22] reconstruct the vertex position ($\vec{x}_i$) from high quality COT and SVX tracks. However, it is important also to measure t_0 and to separate tracks from the vertex that produced the photon from any other vertex that lies close in space but occurs at a different time. This is particularly true at high instantaneous luminosities where two or more collisions can occur in one event and can lie close to each other in z. Misassigned vertex events are a dominant contribution to the background estimate.

To solve this problem, we have developed a new vertex reconstruction algorithm based on track clustering. The procedure [23] uses tracks with a well measured t_0 and z_0 that pass the requirements in Table III and groups those

that are close to each other in both space and time. The algorithm can be separated into three phases: (1) the initial assignment of tracks that are nearby in t_0 and z_0 into clusters, (2) the determination of the t_0, z_0, and Σp_T of the vertex, and (3) the adjustment of the number of clusters by merging clusters that are close to each other.

A simple algorithm is used to make a preliminary assignment of all tracks into clusters. It is designed to overestimate, initially, the number of vertices in the event to obviate the need for dividing a single cluster into two separate clusters, called splitting. The highest-p_T track is designated as the "seed" of the first cluster, and any lower-p_T tracks that lie within three times the typical cluster RMS (0.6 ns and 1.0 cm for t_0 and z_0, respectively) are also assigned to it. The highest-p_T track from the remaining set of tracks is then picked as a second seed and tracks are assigned to it, and so forth until no tracks are left. The mean position and time for each cluster, z_{vertex} and t_{vertex} respectively, is then calculated.

The vertexing algorithm is essentially a likelihood fit using an iterative procedure to get a best estimate of the true number of vertices and their parameters [24]. We allow the cluster parameters to float in the fit and maximize the probability that each track is a member of a vertex with a track density that is Gaussian in both space and time. All clusters are fitted simultaneously. If during the procedure the means of two clusters are within both 3 cm in z_0 and 1.8 ns in t_0 or if two clusters share the same set of tracks, then the clusters are merged. No splitting is done because the initial seeding is designed to overestimate the number of clusters. Splitting a cluster with a too-large RMS can result in two clusters that both do not pass the final requirements and would reduce the clustering efficiency. Having two clusters merged that are close in both space and time does not substantially affect the t_{corr} measurement. We choose the primary vertex for an event to be the highest Σp_T cluster that has at least 4 tracks.

1. Vertexing Resolution and Efficiency

The cluster resolution, the reconstruction efficiency, and beam properties are measured using a high purity $W \rightarrow e\nu$ data sample, selected using the cuts in Table IV. To measure the performance for possible events with photons, the electron track is removed from the vertexing and is used to measure the vertexing performance as it identifies the correct event vertex. Figure 8 shows the z_0 and t_0 distributions as well as their correlation for the vertices in this sample. Both are roughly Gaussian and centered at zero with an RMS of 25 cm and 1.28 ns, respectively, reflecting the accelerator performance. There is a non-Gaussian excess around zero in the z_0 distribution that comes from events that contain more than one vertex. In this case the clustering has merged two vertices that are close to each other, which most likely happens at $z = 0$ cm. The correlation between the collision po-

sition and time distributions is caused by the differences in the proton and anti-proton bunch structure within the accelerator ($\sigma_p \approx 50$ cm and $\sigma_{\bar{p}} \approx 70$ cm [7]).

The vertexing resolution is estimated using a subsample of the events with only one reconstructed vertex. For each event the tracks in the vertex are randomly divided into two groups that are then separately put through the vertexing algorithm. Figure 9 shows the distance between the two clusters, divided by $\sqrt{2}$ to take into account the two measurements, giving a resolution measurement of $\sigma_t = 0.22$ ns and $\sigma_z = 0.24$ cm. The secondary Gaussian in Fig. 9(b) indicates cases where two different vertices have been combined into one cluster. Figure 10 shows the difference in time and position between the reconstructed cluster and the electron track (not included in the vertexing) for the full sample. The distributions are well described by two Gaussians that are both symmetric and centered at zero, indicating no measurement bias. The primary Gaussian distribution contains events where the reconstructed cluster is the vertex that produced the electron. Its RMS is dominated by the resolution of the electron track position and time. The secondary Gaussian distribution contains events where the electron does not originate from the highest Σp_T vertex in the event.

The efficiency of the vertex reconstruction algorithm is investigated using two separate methods. The efficiency as a function of the number of tracks is determined by selecting events that contain a cluster with a high track multiplicity. Next, various random subsets of the tracks are taken that belong to this cluster to see if they alone could produce a cluster. Figure 11 shows the ratio of subset samples in which a cluster is reconstructed to all cases tried for a given set of tracks as a function of the number of tracks in the various subsets. The algorithm is over 90% efficient if 4 tracks are present, where the inefficiency is usually caused by the algorithm reconstructing two separate clusters each with <4 tracks, and 100% efficient with 6 tracks (the final analysis requires at least 4 tracks). A second method that also allows for a measurement of the efficiency as a function of the Σp_T is to consider tracks in a 2 cm × 2 ns window around the electron track ($\sim 5\sigma$ in each direction) and search for clusters. Only events with at most one reconstructed vertex are considered. While this result is not biased by selecting cases with a known vertex, the disadvantage is that for resolution reasons not all tracks are in the window, resulting in a small under-counting of the number of tracks. Figure 11 shows that the efficiency as a function of the number of tracks in the vertex yields a similar result for the two very different methods. This gives confidence in the results as a function of Σp_T. The efficiency plateaus at $\Sigma p_T = 7$ GeV/c, as higher p_T tracks have a better t_0 resolution measurement. It is important to note that the efficiency measurements as a function of the number of tracks are sample-dependent. For instance, if a sample is chosen that is biased towards a higher average track p_T then the efficiency might be higher for a smaller number
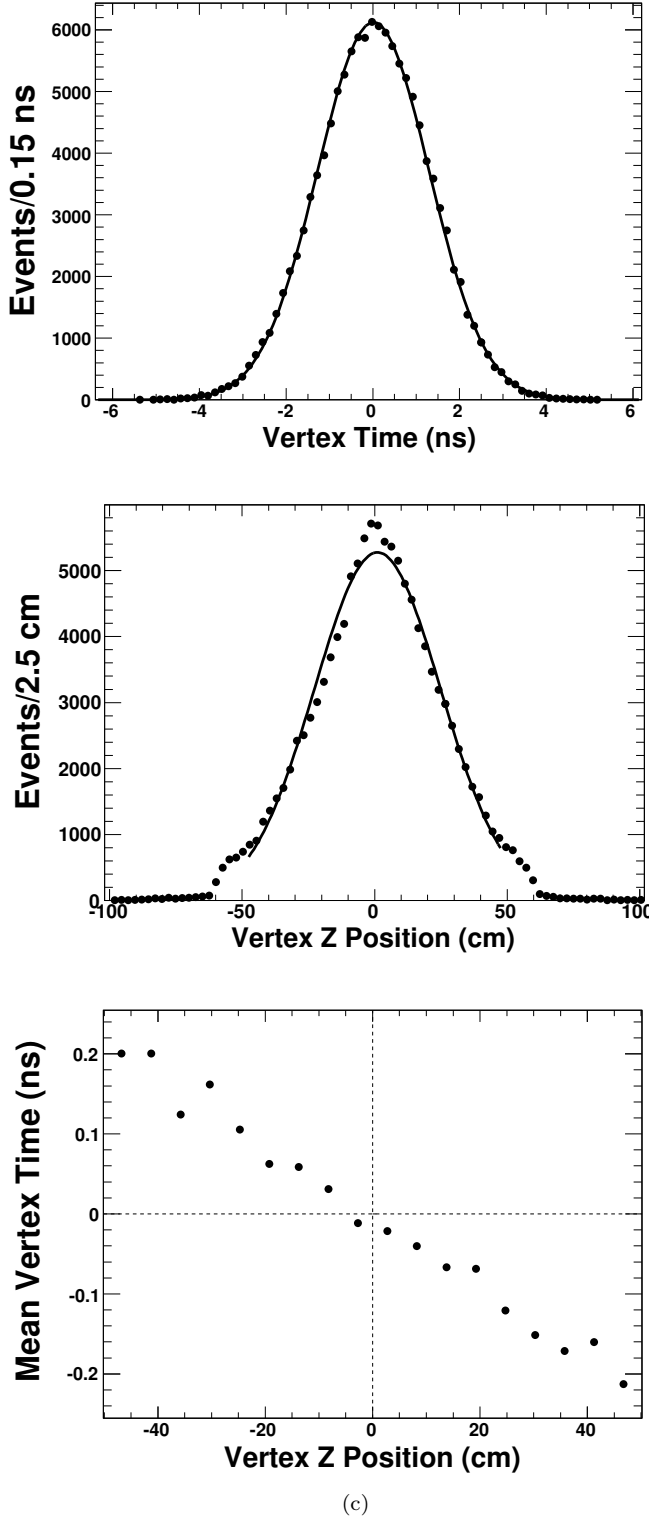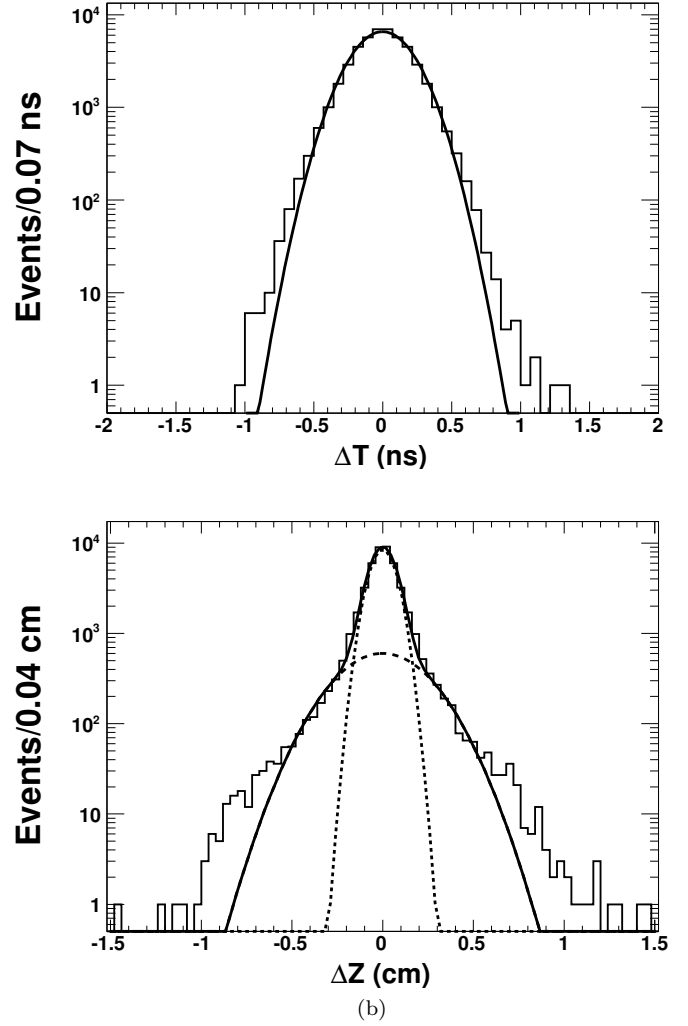
(b)

FIG. 9: The difference in t and z between two arbitrarily selected sets of tracks from the same reconstructed vertex in a $W \rightarrow e\nu$ dataset with the electron track removed from the vertexing. This is a measure of the vertex resolution. (a) is fit with one Gaussian while (b) is fit with two. Note that the factor of $\sqrt{2}$ is already taken out.

of tracks, or if a sample contains many high-p_T tracks, the efficiency as function of Σp_T might plateau earlier. Since the search requires $\Sigma p_T > 15$ GeV/c, as stated later, we take the efficiency for the vertex selection requirements to be 100%.

B. The Corrected Photon Time

With the vertex time and position in hand, we move to a full measurement of t_{corr} by incorporating the EM-Timing information. The time of arrival recorded by the EMTiming system TDCs is corrected using calibrations that take into account channel to channel variations and an energy-dependent ("slewing") effect due to the fixed-threshold discriminators. A full description of the hardware as well as the correction and calibration procedure
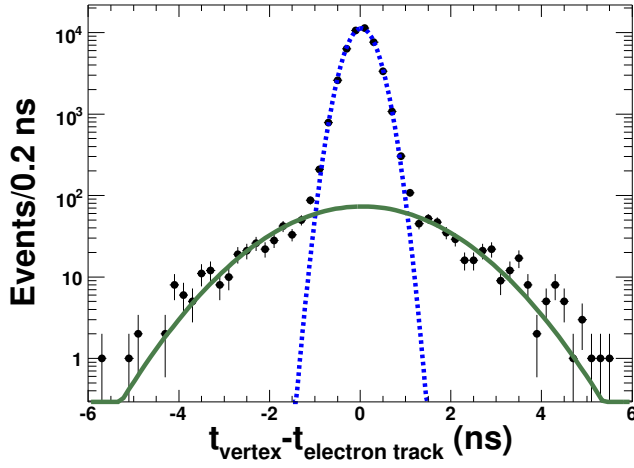

(c)

FIG. 8: Plots (a), (b), and (c) show the t_0, z_0, and their correlation respectively for the reconstructed highest Σp_T vertex in $W \rightarrow e\nu$ events. The fits in (a) and (b) are both a single Gaussian. The falloff in the (b) at $|z| \simeq 60$ cm is due to the requirement that all tracks have $|z| < 70$ cm. In the search the vertex is required to have $|z| < 60$ cm.

(b)
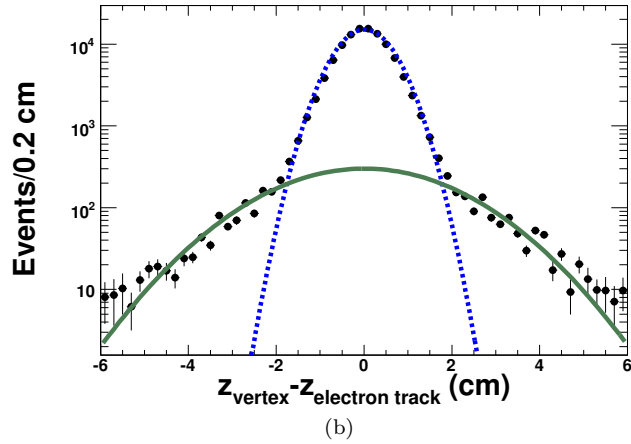
FIG. 10: The difference in t (a) and in z (b) between the electron track and the highest Σp_T reconstructed vertex (without the electron track participating in the vertexing) in $W \to e\nu$ events. The distributions are centered at zero and fit with double Gaussians, indicating that there is no bias in the clustering procedure. The secondary Gaussian contains events where the electron does not originate from the highest Σp_T vertex in the event.

is described in Ref. [16]. The t_{corr} resolution for electrons from $W \to e\nu$ events is 0.64 ns (0.63 ns) for collision data (MC), dominated by the intrinsic resolution (0.5 ns), the precision of the TDC output (0.29 ns) and the vertex t_0 resolution (0.22 ns). A comparison of detector simulation to collision data for $W \to e\nu$ events is shown in Fig. 12. There are no non-gaussian tails out to $\sim 5\sigma$.

III. TRIGGERS, DATASETS AND EVENT PRESELECTION

The event selection is a three stage process. The stages are (1) an online sample is selected (during data taking), (2) a $\gamma + \mathrm{jet} + \not{E}_T$ "preselection sample" is selected offline, and (3) the event selection uses optimized final event selection requirements. The full set of requirements that determine the preselection sample for the search are sum-
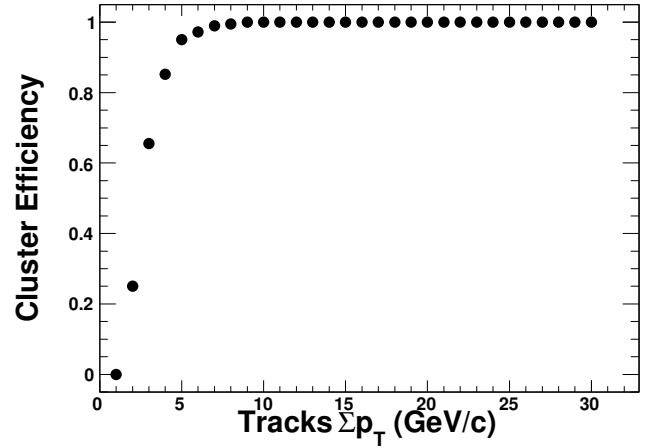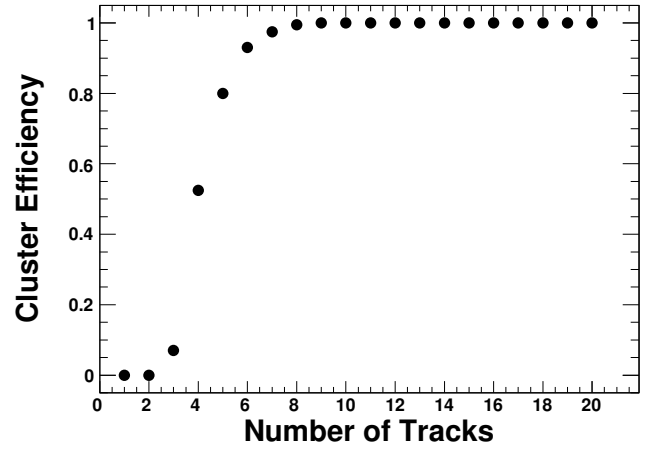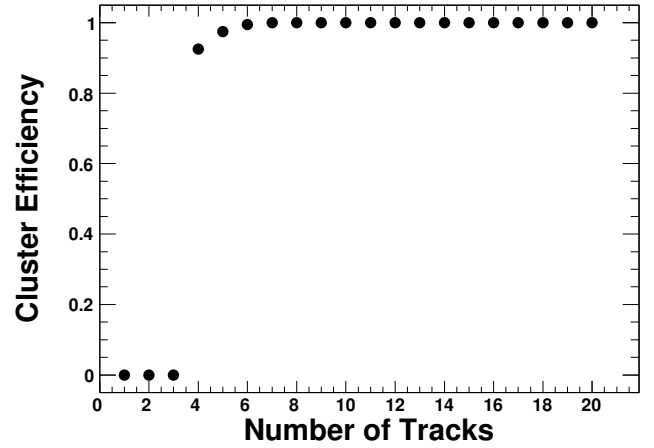

(c)

FIG. 11: The clustering efficiency as a function of the number of tracks using (a) the subset method and (b) the window method, and (c) as a function of the Σp_T of the tracks using the window method. Note that a cluster is required to have at least 4 tracks and the efficiency is 100% for $\Sigma p_T > 15$ GeV/c in this search.
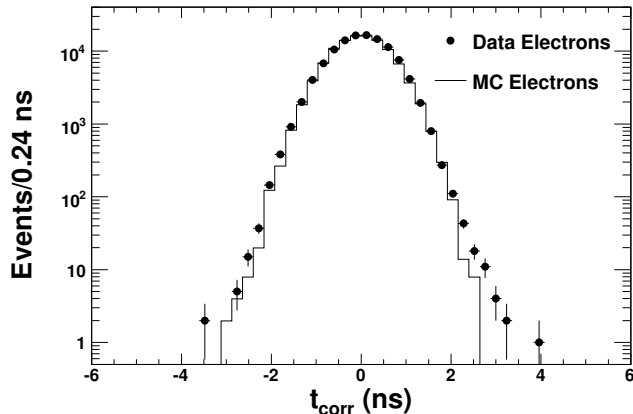
FIG. 12: A comparison between MC (solid) and collision data (points) for $t_{\rm corr}$ for electrons from a $W \to e\nu$ sample. The distributions are well centered around 0 and the resolutions of collision data and MC fit well with a fully corrected RMS of 0.64 ns.

marized in Table V. The optimization and final event requirements are described in Section VI.

The analysis begins by selecting events online using a single set of 3-level trigger requirements that require a photon candidate and $\not{E}_T$. The Level 1 trigger requires a single tower in the calorimeter with $|\eta| < 1.1$, $E_T > 8$ GeV, $E_{\rm Had}/E_{\rm EM} < 0.125$ GeV, and $\not{E}_T > 15$ GeV. For a description of the ID variables, see the Appendix. The Level 2 trigger requires the event to have an EM cluster with $E_T \geq 20$ GeV and $\not{E}_T \geq 15$ GeV. At Level 3 the requirements are tightened with $E_T > 25$ GeV, $E_{\rm Had}/E_{\rm EM} < 0.125$, and $\not{E}_T > 25$ GeV. The data consist of events from the data-taking period from December 2004, when the EMTiming system became fully functional, until November 2005. The data correspond to an integrated luminosity of (570 ± 34) pb^{-1}.

The sample of $\gamma + \not{E}_T$ candidate events that pass the trigger requirements is processed offline where the event characteristics are refined to increase the signal purity and further reduce the backgrounds. The offline preselection requirements include photon ID and $\not{E}_T$ requirements as well as jet, vertex, and cosmic ray rejection requirements. To ensure that all signal events would have passed the trigger with 100% efficiency each event is required to have $\not{E}_T > 30$ GeV, a photon with $E_T > 30$ GeV, and pass the identification criteria shown in Table I.

We require the presence of at least one jet and a high Σp_T vertex in each event for the preselection sample. This preserves the acceptance of $\widetilde{\chi}_2^0\widetilde{\chi}_1^\pm$ and $\widetilde{\chi}_1^+\widetilde{\chi}_1^-$ production while maintaining a search strategy that is as model-independent as possible. While the term "jet" typically refers to the hadronization of a high energy quark or gluon that is produced in the collision, at CDF jets are identified as clusters of energy in the calorimeter. Hence, the hadronic decays of taus and/or the energy deposits from electrons or photons are also effi-

ciently reconstructed as jets. Requiring at least a single jet with $E_T > 30$ GeV and $|\eta| < 2.1$ [15] retains high efficiency and significantly reduces non-collision backgrounds which typically only produce a single photon candidate. As previously mentioned, each event must also have a good space-time vertex with at least 4 good tracks and a Σp_T of at least 15 GeV/c. This allows for a good $t_{\rm corr}$ measurement and further helps reduce the non-collision backgrounds. We also require $|z| < 60$ cm and $|t_0| < 5$ ns for tracks to be included in the vertexing so that both the COT tracking and the calorimeter are able to produce high quality measurements.

A cosmic ray that traverses the detector can create hits in the muon system that are not associated with tracks in the COT and deposit a photon candidate nearby in the calorimeter. An event is rejected from the preselection sample if there are potential cosmic–ray hits in the muon chamber within 30 degrees in ϕ of the photon that are not matched to any track. Table VI lists the cumulative number of events that pass each of the successive requirements to create our preselection sample.

IV. BACKGROUNDS

Backgrounds to the $\gamma + {\rm jet} + \not{E}_T$ signature can be categorized into two different classes: collision and non-collision events. The rate that each type of background contributes to the final signal time-window is estimated solely from collision data using control samples of events that pass all of the final requirements excluding timing. We define the "kinematic sample" as the events that pass the final event requirements (summarized in Section VI, Table IX) except the timing requirement. The $t_{\rm corr}$ distributions outside the timing signal region are used to normalize each background, which is then extrapolated into the signal time region. In this section each of the backgrounds is described, and the signal estimation techniques are outlined.

A. Standard Model Backgrounds: Prompt Photons

Prompt collision events dominate the sample and populate the region around $t_{\rm corr} = 0$ ns. As shown later, it is not important for this search to distinguish further between the various prompt photon sources. Most events are from γj and jj events with one jet reconstructed as a photon and with $\not{E}_T$ from the mis-measurement of the photon and/or jet in the calorimeter. A smaller source is from SM $W \to e\nu +$ jets events where the electron is misidentified as a photon and the ν leaves undetected to cause the $\not{E}_T$. In both cases these events can fall into the large $t_{\rm corr}$ signal time window due to either Gaussian fluctuations of the timing measurement or a wrong collision vertex selection. The latter case dominates the SM background estimate and is more likely at high instantaneous luminosity when there are multiple collision

Photon
$E_T > 30$ GeV and $|\eta| \leq 1.0$
Fiducial: not near the boundary, in ϕ or z, of a
calorimeter tower
$E_{\mathrm{Had}}/E_{\mathrm{EM}} < 0.125$
Energy in a $\Delta R = 0.4$ cone around the photon
excluding the photon energy:
$E^{\mathrm{Iso}} < 2.0$ GeV $+ 0.02 \cdot (E_T - 20$ GeV$)$
No tracks pointing at the cluster or
one track with $p_T < 1.0$ GeV$/c + 0.005 \cdot E_T$
Σp_T of tracks in the
$\Delta R = 0.4$ cone < 2.0 GeV$/c + 0.005 \cdot E_T$
No second cluster in the shower maximum detector
or $E^{2^{\mathrm{nd}}\mathrm{cluster}} < 2.4$ GeV $+ 0.01 \cdot E_T$
$A_{\mathrm{P}} = \frac{|E_{\mathrm{PMT1}} - E_{\mathrm{PMT2}}|}{E_{\mathrm{PMT1}} + E_{\mathrm{PMT2}}} < 0.6$
Jet
$E_T^{\mathrm{jet}} > 30$ GeV
$|\eta^{\mathrm{jet}}| < 2.0$
Highest Σp_T Space-Time Vertex with:
$N_{\mathrm{trks}} \geq 4$
$\Sigma p_T > 15$ GeV$/c$
$|z| < 60$ cm
$|t_0| < 5$ ns
Global Event Cuts
$\not{E}_T > 30$ GeV
Passes cosmic ray rejection requirements

TABLE V: The requirements used to obtain the preselection sample of $\gamma + \mathrm{jet} + \not{E}_T$ events. The cosmic ray rejection cut is described in more detail in [25]. The number of events in the data that pass each cut are shown in Table VI. For more detail on the ID variables, see the Appendix.

Selection	No. of Observed Events
$E_T > 30$ GeV, $\not{E}_T > 30$ GeV,	
photon ID and fiducial requirements	119944
Vertex with $\Sigma p_T > 15$ GeV$/c$, ≥ 4 tracks	19574
≥ 1 jet with $E_T > 30$ GeV and $|\eta| < 2.0$	13097
Cosmics rejection	12855

TABLE VI: Event reduction for the preselection $\gamma + \mathrm{jet} + \not{E}_T$ sample. For the individual requirements see Table V.

vertices reconstructed.

To study the t_{corr} distribution for promptly produced photons, a sample of $W \to e\nu$ events is selected using the requirements described in Table II. This sample is used for the reasons described in Section II, and has the additional advantage that the electron track in the

COT allows for a determination of the correct vertex. To mimic closely the vertexing for events with photons, the electron track is dropped from the vertex clustering. The highest-Σp_T vertex is chosen as the most likely to have produced the EM cluster (the "photon"). Figure 13 shows the resulting t_{corr} distribution and has a double-Gaussian shape. One Gaussian comes from events where the vertex choice is correct and the other Gaussian comes from events where the vertex choice is incorrect [26].

Figure 13 also shows these events separated into right and wrong-vertex subsamples, selected by requiring a tight match ($|z_{\mathrm{track}} - z_{\mathrm{vertex}}| < 2$ cm and $|t_{\mathrm{track}} - t_{\mathrm{vertex}}| < 2$ ns) and anti-match between the electron track and the vertex, respectively. In both cases the distributions are Gaussian and centered at zero. The right vertex selection has an RMS of 0.64 ns, reflecting the system resolution, and the wrong-vertex selection has an RMS of $\sim$2.0 ns. The wrong-vertex time distribution can be understood by combining the RMS of the time distribution without the vertex t_0 and z_0 corrections (RMS= 1.6 ns) with the RMS of the collision t_0 distribution (RMS= 1.28 ns as shown in Fig. 8): $\mathrm{RMS}_{\mathrm{wrong\ vertex}} = \sqrt{1.6^2 + 1.28^2} = 2.05$ ns. The number of events in the t_{corr} signal region ($t_{\mathrm{corr}} > 0$) for prompt, SM sources can thus be estimated by simple extrapolation from a measurement of the timing distribution for $t_{\mathrm{corr}} < 1.2$ ns.

The systematic uncertainty on the number of prompt events in the signal region is dominated by the observed variation in the mean and RMS of the t_{corr} distribution as a function of the $\not{E}_T$, jet E_T, and photon E_T requirements. To estimate the variation, we study the t_{corr} distribution for samples of electrons in $W + \mathrm{jets}$ events for various electron E_T, jet E_T and $\not{E}_T$ event requirements ($20 \leq E_T^{\mathrm{ele}} \leq 40$ GeV$/c^2$, $25 \leq E_T^{\mathrm{jet}} \leq 40$ GeV$/c^2$, and $30 \leq \not{E}_T \leq 50$ GeV). The results are shown in Fig. 14. The variation in the mean is up to 0.1 ns and is conservatively rounded up to 0.2 ns. Similarly, the systematic uncertainty on the RMS of t_{corr} is conservatively overestimated from a fit to Fig. 14 to be 0.02 ns and is only a small addition.

For wrong-vertex assignments, there is an additional variation in the t_{corr} distribution as a function of photon η due to the incorrect time-of-flight calculation. Figure 15 shows the mean and the RMS of the t_{corr} distribution for electrons from $W \to e\nu$ events where the wrong-vertex is selected for the timing correction, as a function of tower-η. We take a systematic uncertainty on the mean and the RMS of the wrong-vertex contribution to the t_{corr} distribution to be equal to the full variation. We assign values of 0.33 ns and 0.28 ns, respectively, to these systematic uncertainties, the latter arising from the largest variations in Fig. 15.

B. Non-Collision Backgrounds

The fraction of non-collision backgrounds in the kinematic sample that fall in the timing signal window is
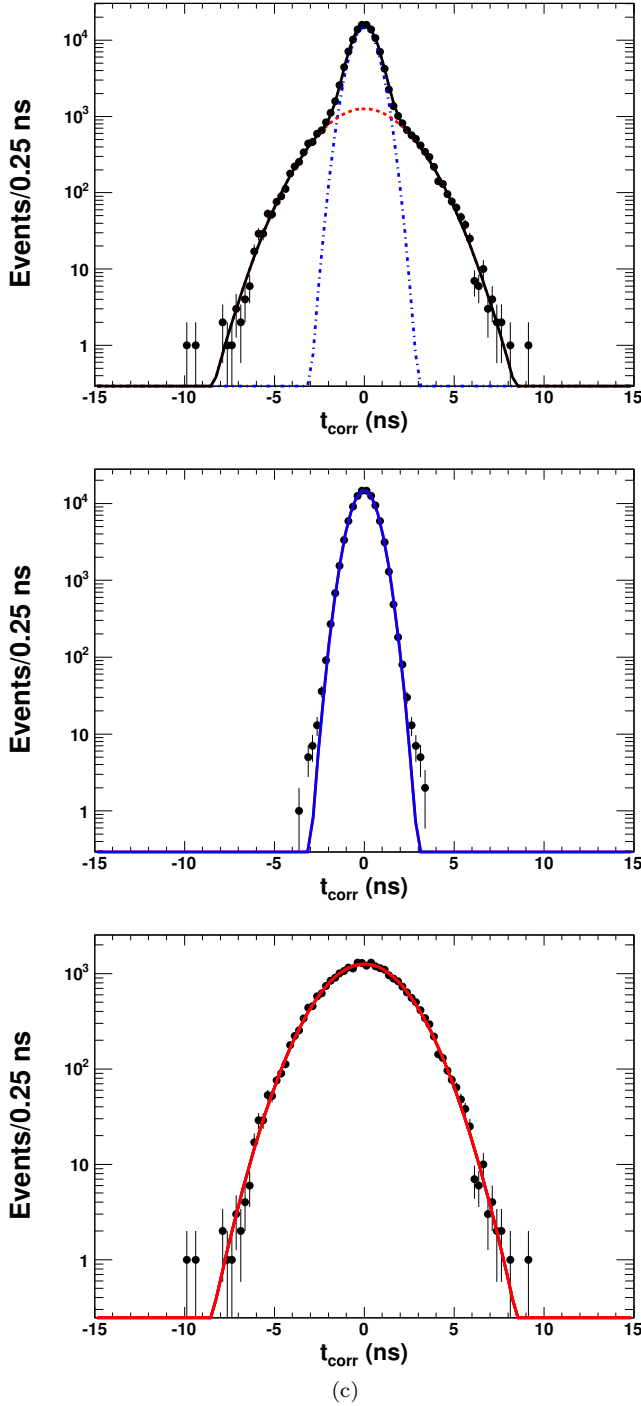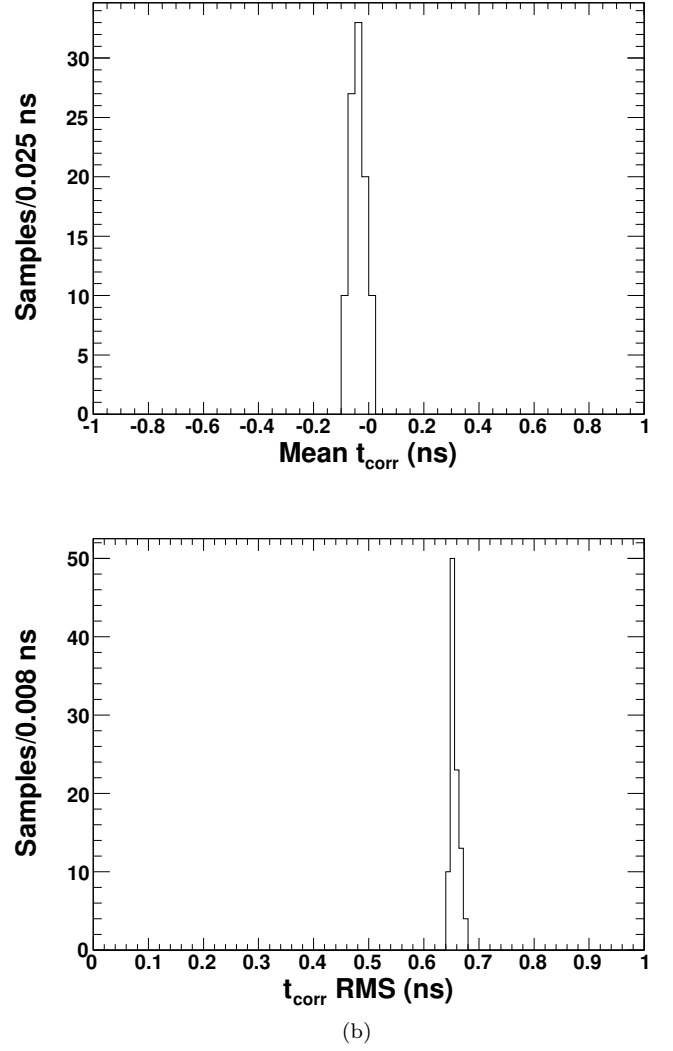
FIG. 14: The mean and RMS of the t_{corr} distribution for electrons from various subsamples of $W \rightarrow e\nu$ + jets events where each entry reflects a different combination of the electron E_T, jet E_T and $\not{E}_T$ event requirements. There are slight shifts as the these requirements vary. While the mean of the distribution is close to zero, the systematic variation on the mean of the primary Gaussian of the prompt time distribution is conservatively taken to be 0.2 ns in the background estimates.

FIG. 13: The t_{corr} distribution for electrons in a sample of $W \rightarrow e\nu$ events. In plot (a) the two Gaussians correspond to the cases when the highest-Σp_T vertex is associated to the electron track and when it is not. These cases can be separated by requiring a match (b) and an anti-match (c), respectively, between the vertex and the electron track in both space and time.

significant. To study these backgrounds, we divide them into two separate sources, cosmic ray muons and beam related backgrounds. Cosmic ray events (cosmics) come from cosmic ray muons that emit photons

via bremsstrahlung as they traverse the detector or produce significant ionization in a large q^2 interaction with the EM calorimeter. Beam halo events (beam halo) are caused by beam particles (mostly from the more intense proton beam) that hit the beam pipe upstream of the detector and produce muons. These muons travel almost parallel to the proton beam direction and shower into the EM calorimeter to create a photon candidate; see Fig. 16. In both cases the event has significant $\not{E}_T$ that is highly correlated with the photon E_T and is uncorrelated with any collision that might occur coincidentally at high luminosity. As cosmic ray muons interact with the detector and produce a photon randomly in time, their time dis-
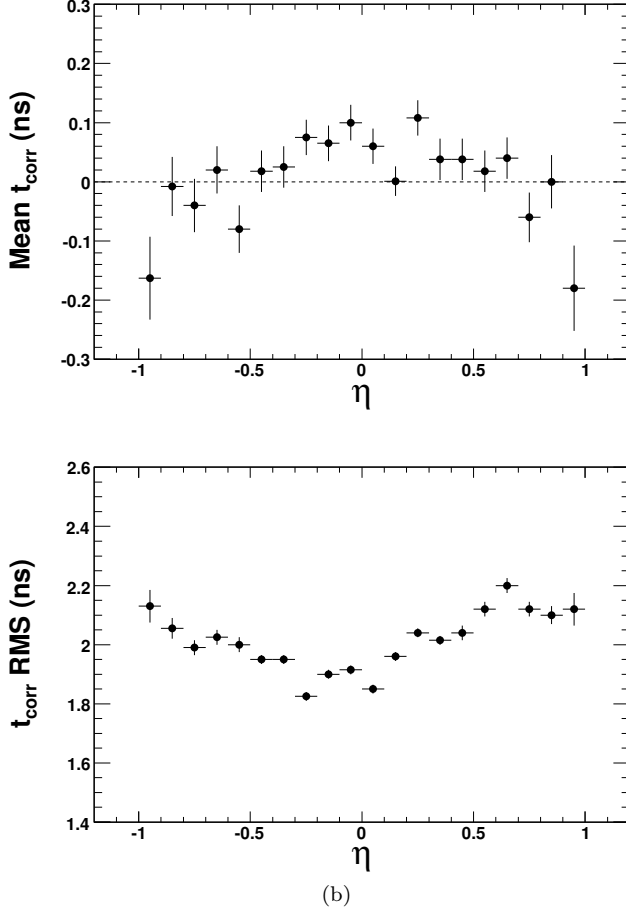
FIG. 15: The mean and RMS of the t_{corr} distribution for electrons from $W \rightarrow e\nu$ events, where the wrong vertex is picked, as a function of η.
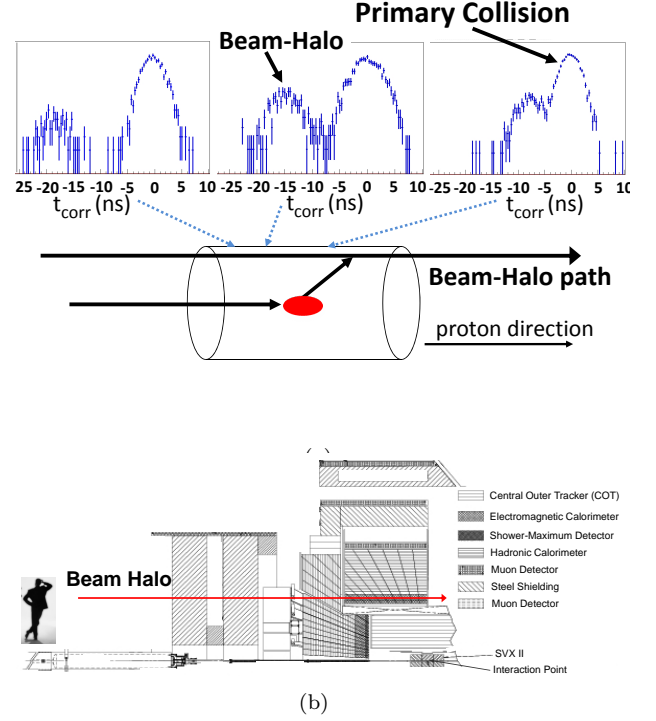

FIG. 16: Illustrations of a beam halo event interacting with the detector. In both figures the muon path is indicated with an arrow. (a) A comparison of the time distributions of prompt collision events with beam halo photon candidates for three example towers in the calorimeter shows that the mean time changes as a function of tower η and is always less than zero. The y-axes are in arbitrary units. (b) An illustration of how the beam halo interacts with the calorimeter. The muon travels through multiple towers in the hadronic calorimeter at high η before hitting the electromagnetic calorimeter.

tribution is roughly constant over the entire calorimeter energy integration window range of 132 ns. Beam halo "photons" typically arrive a few ns earlier than prompt photons for geometric reasons as shown in Fig. 16. However in this case, while the rate is lower, the photon candidate can also have a t_{corr} of $\sim$18 ns (and multiples later and earlier) if the muon was created in one of the bunched beam interactions that can occur every 18 ns in the accelerator.

The rate at which both non-collision backgrounds populate the signal region is estimated from collision data using events with no identified collision. The non-collision sample consists of events with a photon that passes the photon ID criteria listed in Table I, $\not{E}_T > 30$ GeV, and no reconstructed vertex. This sample is used to make timing distribution templates from pure samples of each type of non-collision background. Beam halo events are identified by the energy deposition of the muon as it passes through the high η towers of the plug hadronic calorimeter ($|\eta| \geq 1.1$) and the central EM calorimeter ($|\eta| \leq 1.1$) towers at the same ϕ as the photon candidate; see Fig. 16. The muon deposits a small amount of energy in most towers along its path. Hence, we count

the number of towers in the hadronic calorimeter with ≥ 0.1 GeV and $|\eta| \geq 1.1$ (nHADTowers) and the number of towers in the EM calorimeter with ≥ 0.1 GeV and $|\eta| \leq 1.1$ (nEMTowers). The results are shown in Fig. 17 for the full non-collision sample. Cosmic ray candidates are easily separated from beam halo candidates. This is because cosmics do not deposit energy in the hadronic calorimeter with $|\eta| \geq 1.1$ and typically only deposit significant energy in a single EM tower. An event is identified as a cosmic if it has nHADTowers = 0 and nEMTowers < 5. (Note that we also ignore all photon candidates with $-15° < \phi < 15°$ as beam halo dominates there.) Conversely, beam halo events are identified if they have no muon stubs and have both nHADTowers > 1 and nEMTowers > 4. The t_{corr} distribution for each is shown in Fig. 18 for the entire calorimeter energy integration window and indicates that the real collision contamination is negligible. As these events lack a vertex, the photon arrival time is corrected assuming $z_0 = 0$ and $t_0 = 0$ in Eq. 1. To create the t_{corr} distribution for use in extrapolating the number of non-collision events in the signal time window from the control regions, we convolute the distributions in Fig. 18 with the
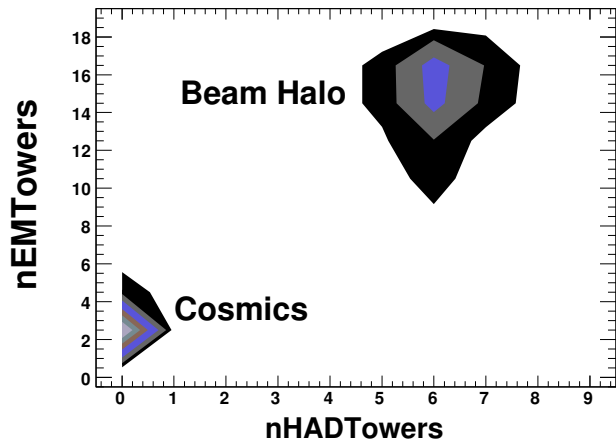
FIG. 17: The variables used to separate cosmic and beam halo backgrounds in the $\gamma + \cancel{E}_T$ sample without a vertex. Beam halo muons deposit energy in many HAD towers as they interact with the detector at high η and many EM towers as they traverse the central portion of the calorimeter along the beam halo direction.

RMS of the interaction time of 1.3 ns as the collision time is uncorrelated. As will be seen, the uncertainty on the rate of the number of events in the signal time region is dominated by the statistical uncertainty on the number of non-collision events in the control regions. We note that because of the accelerator geometry there are ~ 40 times more beam halo events that occur around the region $\phi \simeq 0°$ as can be seen in Fig. 19. This explains the $-15° < \phi < 15°$ separation requirement and will be further used in the final background estimate procedure.

C. Background Estimation Methods

The number of background events in the signal region is estimated from collision data by fitting a set of control regions with background timing shapes and extrapolating into the signal time window. The t_{corr} distribution shape "templates" for each background source are given in Figs. 13 and 18. Since a sample is defined by kinematic cuts alone we can estimate the number of background events in any potential signal time window using sensibly chosen control regions. Thus, we can predict the background rate for a large variety of final kinematic and timing cuts and use these estimates as part of our optimization procedure.

The background prediction for the signal timing region for each subsample of $\gamma + \mathrm{jet} + \cancel{E}_T$ events after the kinematic sample requirements is done as a two-step process with multiple control regions. There are a number of reasons for this. Multiple control regions are used to get a robust estimate of each of the background event contributions that are hard to separate; for example the timing region $\{-15, 0\}$ ns is populated by both the wrong-vertex backgrounds and beam-halo backgrounds. Sec-
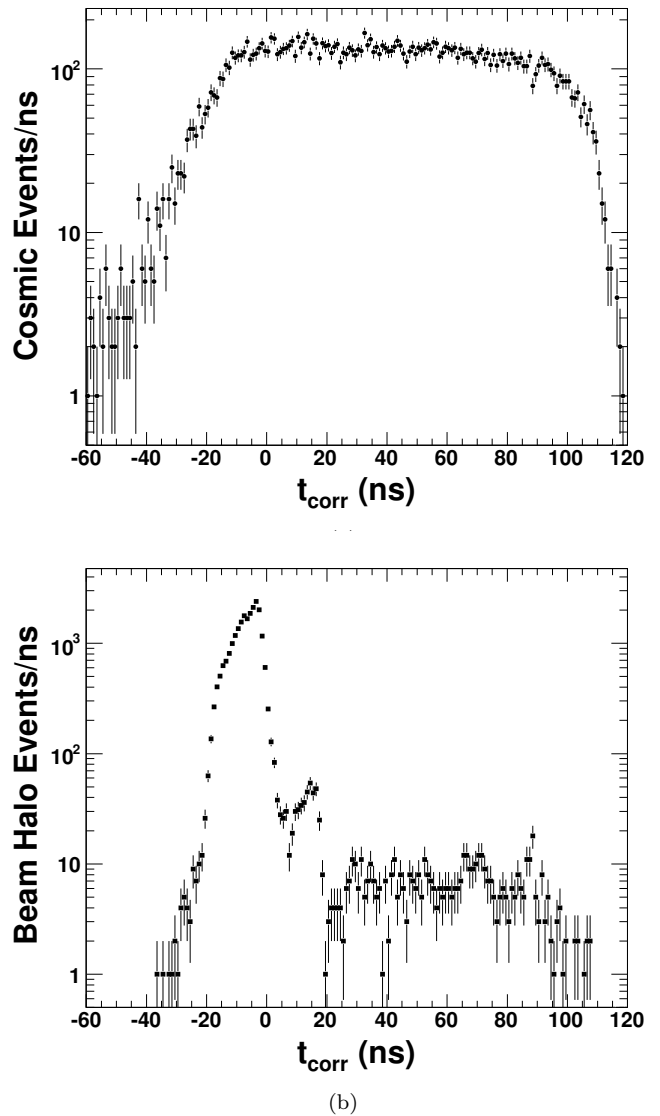

(b)

FIG. 18: The t_{corr} distributions for the cosmic ray (a) and beam halo (b) backgrounds in the $\gamma + \cancel{E}_T$ sample without a collision.

ondly, for many of the potential kinematics-only samples, low statistics can bias the fit results. We define a set of control regions chosen such that each is largely dominated by a single background source, and use an iterative fitting procedure to ensure that each background is well estimated for each kinematic requirement choice during optimization.

The control regions are designed to allow for a good estimation of each background separately. Since the cosmics rate is essentially constant in time, the time control region is defined to be $\{25, 90\}$ ns and is chosen such that (a) it is well above the beam halo secondary peak at ~ 18 ns and (b) it does not include the region close to the end of the calorimeter energy integration window where the event rate falls sharply. The beam halo control region is defined to be $\{-20, -6\}$ ns and is chosen such that (a) it contains most of the beam halo events
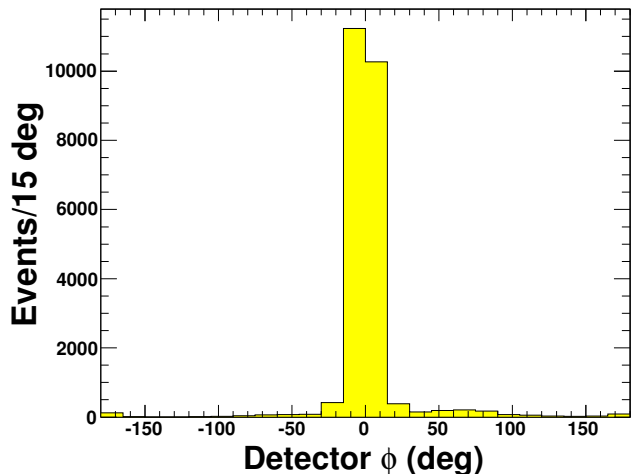
FIG. 19: The number of beam halo photon candidates as a function of detector ϕ. Most photons arrive at $\phi \approx 0$.

but (b) stays well away from the region dominated by the prompt photon production. The standard model control region is defined to be $\{-10, 1.2\}$ ns. An additional requirement on this region is that the photon must have $|\phi| \geq 15°$. This allows us (a) to include as much of the collision data as possible to get good precision on the ratio of right to wrong-vertex events, (b) allows for a potential signal region above 1.2 ns, and (c) removes most of the beam halo contamination. We note that while the ϕ restriction is useful for estimating backgrounds, it is not an effective tool in improving the sensitivity. While the upper time limit of the signal region at 10 ns is not quantitatively motivated, it contains most of a long-lived signal on the order of nanosecond lifetimes as the time distribution falls exponentially (Fig. 2).

The background prediction for the signal timing region for each subsample of $\gamma + \text{jet} + \not{E}_T$ events after the kinematic sample requirements is done as a two-step process. In step 1, the wrong-vertex fraction and the overall prompt photon rate are measured using the collision data control sample after a correction for non-collision contamination. The non-collision contamination to the control sample is estimated by fitting the beam halo template and cosmics, simultaneously in the control regions $\{-20, -6\}$ ns (beam halo dominated) and $\{25, 90\}$ ns (cosmics dominated). The fit is extrapolated to the collision control region $\{-10, 1.2\}$ ns, where the non-collision contamination is subtracted off. The remaining data are then fit using the two single Gaussian functions as shown in Fig. 13. While the mean and RMS of both functions are fixed, the normalizations are allowed to float. After fitting, the final normalization is scaled by a factor of $12/11$ to account for the removed data in the 30° slice around $\phi = 0$. The statistical error on the prediction in the signal region is determined by the fit. The uncertainty on the number of events in the signal time window is estimated by varying the collision background fractions, means, and RMS's according to their systematic

and statistical uncertainties. We note that if we choose the kinematic sample to be the dataset that passes the preselection sample criteria (see Table V), the resulting fraction of wrong-vertex events is $(3\pm1)\%$.

In step 2, the rate of the non-collision backgrounds is estimated using the entire ϕ region. In the full data sample a simultaneous fit is performed for the normalization of the beam halo and cosmic ray backgrounds using the control regions, after subtracting off the expected contamination from collision sources in both regions obtained in step 1. The uncertainties on this estimate are dominated by the statistical error on the number of events in the control regions and the uncertainty on the extrapolation from the prompt background. With this technique, the background estimation for all sources is robust enough to be applied to a variety of kinematic requirements. This feature will be used along with the simulated acceptance of GMSB events for the optimization.

V. ACCEPTANCES FOR GMSB EVENTS AND THEIR SYSTEMATIC UNCERTAINTIES

We use MC techniques to estimate the acceptance and overall sensitivity to GMSB models. The sparticle properties (mass, branching fractions etc.) are calculated with ISASUGRA [27]. Samples of events of GMSB processes are simulated according to their production cross sections using PYTHIA [18], a full detector simulation, as well as parton distribution functions (PDFs) [28]. All sparticle production mechanisms are simulated as this maximizes the sensitivity to the model [29]. To map out the sensitivity for GMSB models as a function of $\widetilde{\chi}_1^0$ mass and lifetime, MC samples are generated for $65 \leq m_{\widetilde{\chi}_1^0} \leq 150$ GeV/c^2 and $0 \leq \tau_{\widetilde{\chi}_1^0} \leq 40$ ns. As ~5% of the simulated events pass all the selection requirements, the size of the MC samples is chosen to be 120,000 events so that their statistical uncertainty is ~1% and negligible compared to the combined systematic uncertainty.

The total event acceptance is

$$A \cdot \epsilon = (A \cdot \epsilon)_{\text{Signal MC}} \times C_{\text{MC}}, \qquad (3)$$

where the MC program is used to estimate A, the fraction of events that pass the kinematic sample requirements and to estimate ϵ, the fraction of these events that remain after the t_{corr} requirement. C_{MC} is a correction factor for efficiency loss due to the cosmic ray rejection requirement and is not simulated. Table VII shows the breakdown of the number of MC events after each of the preselection sample requirements in Table V for an example GMSB point at $m_{\widetilde{\chi}_1^0} = 100$ GeV/c^2 and $\tau_{\widetilde{\chi}_1^0} = 5$ ns, near the expected sensitivity limit.

The loss of signal events due to the cosmic ray rejection requirement is chiefly caused by real cosmic rays overlapping the signal events and causing the requirement to fail. This efficiency is estimated simply to be equal to the efficiency of the requirement as measured from the preselec-

Requirement	Events passed	$(A \cdot \epsilon)_{\text{Signal MC}}$ (%)
Sample events	120000	100.00
Central photon with		
$E_T > 30$ GeV, and		
$\not{E}_T > 30$ GeV	64303	53.6
Photon fiducial and ID cuts	46730	38.9
Good vertex	37077	30.9
≥ 1 jet with $E_T > 30$ GeV		
and $|\eta| < 2.0$	28693	23.9
Cosmic ray rejection $(\times C_{\text{MC}})$	N/A	23.5

TABLE VII: Summary of the MC event reduction for a GMSB example point at $m_{\widetilde{\chi}_1^0} = 100$ GeV/c^2 and $\tau_{\widetilde{\chi}_1^0} = 5$ ns as a function of the preselection sample cuts of Table V. Note that the efficiency loss caused by the cosmic ray rejection requirement is implemented as an MC correction factor, C_{MC}.

tion sample but additionally requiring the photons to be within $|t_{\text{corr}}| < 10$ ns to select collision events with high purity. There are 12,583 events in this sample. 12,360 events remain after the cosmic ray rejection requirement, giving an efficiency of $C_{\text{MC}} = \frac{12,360}{12,583} = (98 \pm 1)\%$, with the error conservatively overestimated.

The systematic uncertainty that enters the limit calculation (and thus a proper optimization) is dominated by the potential shift of the t_{corr} measurement for the kinematic sample requirements. This along with the remaining systematic effects on the acceptance, luminosity, and production cross section are summarized in Table VIII. The uncertainty is evaluated at $m_{\widetilde{\chi}_1^0} = 95$ GeV/c^2 and $\tau_{\widetilde{\chi}_1^0} = 10$ ns. The effect of varying $m_{\widetilde{\chi}_1^0}$ and $\tau_{\widetilde{\chi}_1^0}$ is negligible when compared to the other systematic effects. We next describe the estimation of these important effects.

- *Time measurement:* There is an uncertainty on the acceptance due to the systematic variations in the t_{corr} measurement shown in Fig. 13. Three types of uncertainties are considered simultaneously: (1) a shift in the mean of t_{corr} measurement, (2) a change in the RMS variation of the t_{corr} measurement, and (3) a change in the fraction of events that have an incorrectly chosen vertex. The variation of the mean of the right (wrong) vertex t_{corr} measurement has been conservatively overestimated to be 0.2 ns (0.33 ns) and can shift events into and out of the signal region. The fractional variation in acceptance due to this effect is estimated to be 6.7%. The fractional change in acceptance due to changing the RMS of the t_{corr} measurement is estimated to be 0.03%. The variation due to fluctuations in the number of additional vertices, is $\sim 1.5\%$ [30]. Taken in quadrature the total uncertainty is 6.7% and forms the dominant contribution to the systematic uncertainty on the acceptance.

- *Photon ID efficiency:* As described in Section II, the systematic uncertainty on the photon ID efficiency is estimated to be 5%.

- *Jet energy:* As the event selection requires a jet with $E_T > 30$ GeV a systematically mismeasured jet can contribute to the acceptance uncertainty. We use the standard CDF procedure [15] of varying the jet energy by $\pm 1\sigma$ of the estimated energy systematic uncertainty and find the resulting variation in the acceptance to be 1.0%.

- *Initial and final state radiation:* The uncertainty in the MC simulation of ISR and FSR effects can cause the photon, the jet, or the $\not{E}_T$ to be systematically more likely to pass or fail the kinematic sample requirements and affect the acceptance. This is estimated using the standard CDF procedure of varying the ISR/FSR parameters as described in [22]. The systematic variation in the acceptance is estimated to be 2.5%.

- *Parton distribution functions (PDFs):* The production cross section and the acceptance have uncertainties due to uncertainty in the PDFs. The uncertainty is estimated using the standard CDF procedure of varying the PDFs within the uncertainties provided by CTEQ-6M as described in [28]. We find a relative uncertainty of 0.7% on the acceptance and 5.9% on the cross section.

- *Renormalization scale:* There is a systematic uncertainty of the NLO production cross section which is estimated using the standard technique of varying the renormalization scale between $0.25 \cdot q^2$ and $4 \cdot q^2$ using PROSPINO2 [31]. The variation of the cross section is estimated to be 2.4%.

Factor	Relative Systematic Uncertainty (%)
Acceptance:	
t_{corr} measurement and vertex selection	6.7
Photon ID efficiency	5.0
Jet energy scale	1.0
Initial and Final State Radiation	2.5
Parton Distribution Functions	0.7
Total	8.8
Cross section:	
Parton Distribution Functions	5.9
Renormalization scale	2.4
Total	6.4
Luminosity	6.0

TABLE VIII: Summary of the systematic uncertainties on the acceptance and the total production cross section.

VI. OPTIMIZATION AND EXPECTED SEARCH SENSITIVITY

The sensitivity to sparticle production is estimated in the form of the expected 95% C.L. upper cross section limits (σ_{95}^{exp}) for various points in parameter space. Before unblinding the signal region in the data we optimize the search sensitivity and determine the best event selection requirements for a prospective GMSB signal. This is done using the background rates and the signal acceptances for all sparticle production, with uncertainties, available for different sets of selection requirements. The procedure is to consider the number of events "observed" in a pseudo-experiment, N_{obs}, assuming no GMSB signal exists, and to calculate $\sigma_{95}(N_{\text{obs}})$ using a Bayesian method with a constant cross section prior [32]. The uncertainties on the signal efficiencies, backgrounds, and luminosity are treated as nuisance parameters with Gaussian probability distributions. We write $\sigma_{95}(N_{\text{obs}}, \text{cuts})$ since the limit is also a function of the number of predicted background events and $A \cdot \epsilon$, where both factors depend on the set of requirements (cuts) used.

The expected cross section limit is calculated from $\sigma_{95}(N_{\text{obs}}, \text{cuts})$ and takes into account the outcomes of the pseudo-experiments determined by their relative Poisson probability [33], $\mathcal{P}$. The expected cross section limit and its RMS are given by:

$$\sigma_{95}^{\text{exp}}(\text{cuts}) = \sum_{N_{\text{obs}}=0}^{\infty} \sigma_{95}(N_{\text{obs}}, \text{cuts})$$
$$\cdot \mathcal{P}(N_{\text{obs}}, \mathcal{N}_{\text{back}}(\text{cuts})) \quad (4)$$

$$\text{RMS}^2(\text{cuts}) = \sum_{N_{\text{obs}}=0}^{\infty} (\sigma_{95}(N_{\text{obs}}, \text{cuts}) - \sigma_{95}^{\text{exp}}(\text{cuts}))^2$$
$$\cdot \mathcal{P}(N_{\text{obs}}, \mathcal{N}_{\text{back}}(\text{cuts})), \quad (5)$$

where $N_{\text{back}}(\text{cuts})$ is the number of expected background for a given set of cuts and $\mathcal{P}(N_{\text{obs}}, \mathcal{N}_{\text{back}}(\text{cuts}))$ is the normalized Poisson distribution of N_{obs} with a mean $N_{\text{back}}(\text{cuts})$. The expected maximal sensitivity for each GMSB parameter choice is found when the set of requirements minimizes $\sigma_{95}^{\text{exp}}(\text{cuts})$. To find the minimal σ_{95}^{exp} we simultaneously vary the photon E_T, $\not{E}_T$, and jet E_T thresholds, $\Delta\phi(\not{E}_T, \text{jet})$, and the lower limit on t_{corr}. Here $\Delta\phi(\not{E}_T, \text{jet})$ is the azimuthal angle between $\not{E}_T$ and the highest-E_T jet. This angle cut helps reject events where the $\not{E}_T$ is overestimated because of a poorly measured jet. The upper limit on t_{corr} is kept constant at 10 ns. As an illustration of the optimization, Fig. 20 shows the expected cross section limit for a GMSB example point [12] at $m_{\widetilde{\chi}_1^0} = 100$ GeV/c^2 and $\tau_{\widetilde{\chi}_1^0} = 5$ ns as a function of the lower t_{corr} requirement. All other requirements are kept fixed at their optimized values. This point is close to the boundary of the exclusion region.

In the region $65 < m_{\widetilde{\chi}_1^0} < 150$ GeV/c^2, $0 < \tau_{\widetilde{\chi}_1^0} < 40$ ns the optimal cut values have negligible variation except for a small variation in the optimal jet E_T requirements and

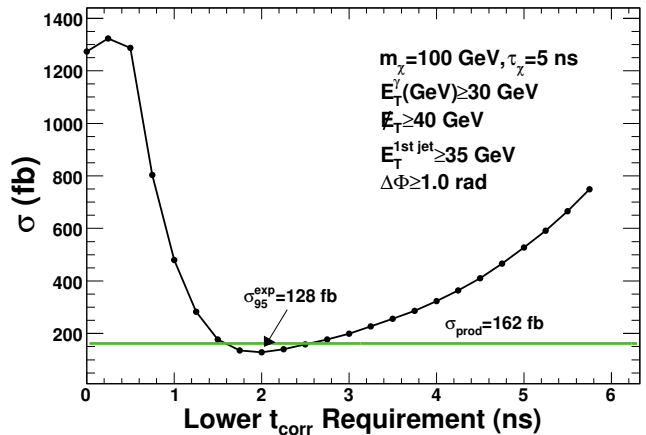FIG. 20: The expected 95% C.L. cross section limit as a function of the lower value of the t_{corr} requirement for a GMSB example point with $m_{\widetilde{\chi}_1^0} = 100$ GeV/c^2 and $\tau_{\widetilde{\chi}_1^0} = 5$ ns. The values of the kinematic sample requirements are held at their optimized values.

the lower limit on t_{corr}. A single fixed set of final requirement values is chosen since, far from the expected exclusion boundaries, this results in at most a 4% loss of sensitivity. The final values are Photon $E_T > 30$ GeV, jet $E_T > 35$ GeV, $\Delta\phi(\not{E}_T, \text{jet}) > 1.0$, $\not{E}_T > 40$ GeV, and $2 < t_{\text{corr}} < 10$ ns. For $m_{\widetilde{\chi}_1^0} = 100$ GeV/c^2 and $\tau_{\widetilde{\chi}_1^0} = 5$ ns we find an acceptance of $(6.3 \pm 0.6)\%$. Table IX gives more details on the acceptance reduction as a function of the requirements. Our fit to the data outside the signal region predicts total backgrounds of 6.2 ± 3.5 from cosmic rays, 6.8 ± 4.9 from beam halo background sources, and the rest from the standard model with a measured wrong-vertex fraction of $(0.5 \pm 0.2)\%$. Inside the signal region, $2 < t_{\text{corr}} < 10$ ns, we predict 1.25 ± 0.66 events: 0.71 ± 0.60 from standard model, 0.46 ± 0.26 from cosmic rays, and 0.07 ± 0.05 from beam halo. Table X shows the various possible number of "observed" events and their probability in the no-signal hypothesis. We find for this point in parameter space $\sigma_{95}^{\text{exp}} = 128$ fb with an RMS of 42 fb. The total sparticle production cross sections, σ_{prod}, are calculated at next to leading order (NLO) by multiplying the LO production cross section from PYTHIA [18] by the theoretical K-factors from [34] ($\sim$1.2 for this mass range). A total sparticle production cross section of 162 fb is predicted for this point, and thus we expect to exclude it. A total of 5.7 ± 0.7 signal events is expected for this mass/lifetime combination.

VII. DATA, CROSS SECTION LIMITS AND FINAL RESULTS

After the kinematic requirements (Table IX) 508 events remain in the data sample. Table XI lists the number of events observed in the three control regions. Figure 21 shows the t_{corr} distribution from data along

Preselection Sample Requirements	Individual Efficiency (%)	Cumulative Efficiency (%)
$E_T^\gamma > 30$ GeV, $\not{E}_T > 30$ GeV	54	54
Photon ID and fiducial, $|\eta| < 1.0$	74	39
Good vertex,		
$\quad \sum_{\text{tracks}} p_T > 15$ GeV/c	79	31
$|\eta^{\text{jet}}| < 2.0$, $E_T^{\text{jet}} > 30$ GeV	77	24
Cosmic ray rejection	98	23
Requirements after		
Optimization		
$\not{E}_T > 40$ GeV, $E_T^{\text{jet}} > 35$ GeV	92	21
$\Delta\phi(\not{E}_T, \text{jet}) > 1.0$ rad	86	18
2 ns $< t_{\text{corr}} < 10$ ns	33	6

TABLE IX: The data selection criteria and the total, cumulative event efficiency for an example GMSB model point at $m_{\tilde{\chi}_1^0} = 100$ GeV/c^2 and $\tau_{\tilde{\chi}_1^0} = 5$ ns. The listed requirement efficiencies are in general model-dependent. The good vertex requirement (95% efficient) includes the $|z_0| < 60$ cm cut. The efficiency of this cut, as well as that of the photon fiducial and cosmic ray rejection cuts, is model-independent and estimated from data.

N_{obs}	$\sigma_{95}(N_{obs})$ (fb)	Probability (%)
0	79.9	28.7
1	120	35.8
2	153	22.4
3	196	9.32
4	239	2.91
5	280	0.729

TABLE X: The 95% C.L. cross section limit as a function of the hypothetically observed number of events, the Poisson probability for the number of events based on the no-signal hypothesis (1.3 events expected) at an example GMSB point of $m_{\tilde{\chi}_1^0} = 100$ GeV/c^2 and $\tau_{\tilde{\chi}_1^0} = 5$ ns, and the requirements listed in Table IX. We find for this point in parameter space $\sigma_{95}^{\text{exp}} = 128$ fb with an RMS of 42 fb. A total sparticle production cross section of 162 fb is predicted for this point, and thus on average we expect to exclude it.

Control Region	Dominant Background	Observed Events
$-20 \le t_{\text{corr}} \le -6$ ns	Beam halo	4
$-10 \le t_{\text{corr}} \le 1.2$ ns	SM	493
$25 \le t_{\text{corr}} \le 90$ ns	Cosmics	4

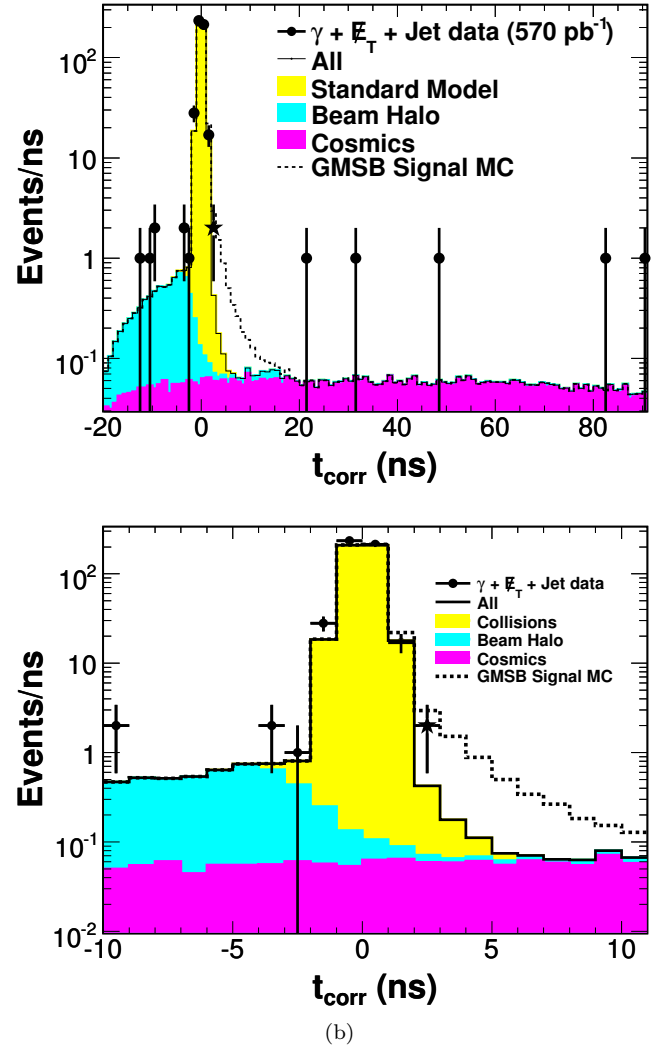TABLE XI: The observed number of events in each control region after all the optimized kinematic sample requirements.

(b)

FIG. 21: The t_{corr} distribution including the control and signal regions, after all but the timing cut for all backgrounds, for the expected signal and the observed data. A total of 508 events is observed in the full time window. The two observed events in the signal region, $2 < t_{\text{corr}} < 10$ ns, are in the first signal time bin (marked with a star). This is consistent with the background expectation of 1.3±0.7 events.

with the signal expectations and the background shapes, normalized using the control regions.

Since the number of events in the timing window $1.2 \le t_{\text{corr}} \le 10$ ns is predicted by the background estimation techniques we can compare the number of predicted and observed events. Table XII shows the results as each of the optimized requirements is applied sequentially along with the expectations for a GMSB example point. The large fractional errors on the backgrounds are due to the systematic uncertainty on the mean and RMS of the SM distributions as discussed in Section IV. The large fractional errors on the beam halo and cosmic ray estimates are primarily due to the small number of events in the control regions. Neither is a problem in the final analysis as the absolute number of background events is small in the signal region. After each requirement, sparti-

cle production would have increased the number of events observed in the signal region above the background levels. However, there is good agreement between the background prediction and the number of events observed in all cases. The bulk of the beam halo and cosmics background are rejected by the timing requirement.

There are 2 events in the final signal region, $2 < t_{\rm corr} < 10$ ns, consistent with the background expectation of 1.3 ± 0.7 events. Figure 21(b) shows in detail the time window immediately around the signal region. The data is consistent with background expectations. The two events have $t_{\rm corr}$ of 2.2 ns and 2.6 ns respectively. Figure 22 shows the distributions for the background and signal expectations along with the data as functions of the photon E_T, jet E_T, $\not{E}_T$, and $\Delta\phi(\not{E}_T, {\rm jet})$ requirements. There is no distribution that hints at an excess.

A model-independent exclusion limit can be assigned based on this non-observation. The two observed events and the background and its uncertainty give a 95% C.L. upper limit ($N_{95}^{\rm obs}$) on the number of events produced of $N_{95}^{\rm obs} = 5.2$ events. Any model of new physics that predicts more than this number of delayed $\gamma + {\rm jet} + \not{E}_T$ events is excluded. To make our results useful for future model builders to calculate cross section limits for other acceptance models, we calculate a correction factor, $C_{\rm sys}$, that takes into account the systematic uncertainties on the acceptance, efficiency and the luminosity, which are also fairly model-independent. Using the relation

$$\sigma_{95}^{\rm obs} = \frac{N_{95}^{\rm obs} \cdot C_{\rm sys}}{\mathcal{L} \cdot (A \cdot \epsilon)} \qquad (6)$$

and the methods to calculate $\sigma_{95}^{\rm obs}$, we find $N_{95}^{\rm obs} \cdot C_{\rm sys} = 5.5$ events.

A. Cross Section Limits and Exclusion Regions for GMSB Production

To compare our results to GMSB models we calculate the 95% C.L. upper limits and compare to GMSB production cross sections. To allow for a more detailed comparison to production cross sections for any other model that predicts heavy, long-lived, neutral particles that produce the $\gamma + {\rm jet} + \not{E}_T$ final state [35] we parametrize the acceptance using variables that are largely independent of the GMSB specific dynamics.

There are several effects that cause the acceptance to vary as a function of both the $\widetilde{\chi}_1^0$ mass and lifetime. The dominant ones are the probability that (a) at least one $\widetilde{\chi}_1^0$ of the two decays in the detector volume to produce a photon that passes the kinematic sample selection criteria ($P_{\rm vol}$) and that (b) $t_{\rm corr}$ is within the signal time window (P_t). We find these are roughly independent of each other, and define $A \cdot \epsilon = P_{\rm vol} \cdot P_t \cdot P_{\rm corr}$, where $P_{\rm corr}$

is a minor correction described below. We find:

$$P_{\rm vol} = (-0.254 + 6.85 \cdot 10^{-3} m_{\widetilde{\chi}_1^0} - 1.54 \cdot 10^{-5} m_{\widetilde{\chi}_1^0}^2)$$
$$\cdot (1 - e^{-\frac{-0.625 + 0.0647 \cdot m_{\widetilde{\chi}_1^0}}{\tau_{\widetilde{\chi}_1^0} + 0.842}}) \quad (7)$$
$$P_{\rm t} = (-0.0449 + 8.69 \cdot 10^{-3} m_{\widetilde{\chi}_1^0} - 3.49 \cdot 10^{-5} m_{\widetilde{\chi}_1^0}^2)$$
$$\cdot (1 - (1 - e^{\frac{-4.78}{\tau_{\widetilde{\chi}_1^0} + 1.21}})^2) \quad (8)$$

where each function consists of two multiplicative terms: a mass-dependent term that determines the overall scale, and a lifetime dependent term. Here $m_{\widetilde{\chi}_1^0}$ is in GeV/c^2 and $\tau_{\widetilde{\chi}_1^0}$ is in ns. The small mass dependency of the overall scale and of the exponential term in $P_{\rm vol}$ both come from variations in the $\widetilde{\chi}_1^0$ boost with its mass in production [14]. A higher $\widetilde{\chi}_1^0$ boost can cause the $\widetilde{\chi}_1^0$ to leave the detector with a higher probability given its lifetime and cause the photon to be emitted at smaller angles relative to the $\widetilde{\chi}_1^0$ direction such that its arrival time becomes similar to a promptly produced photon. A variation in the boost is caused by a change in the shape of the p_T distribution as a function of the $\widetilde{\chi}_1^0$ mass. Another important, but non-dominant, factor is the lifetime term in the denominator of both exponentials. This takes into account the effect that both the acceptance and efficiency are not zero at low $\widetilde{\chi}_1^0$ lifetimes but have a finite contribution due to the resolution of the $t_{\rm corr}$ measurement. This causes prompt photons to fluctuate into the signal time window. An additional lifetime dependent correction term, $P_{\rm corr}$, is introduced to compensate for remaining small deviations in $A \cdot \epsilon$:

$$P_{\rm corr} = 1.04 - \frac{0.2}{55.0} \tau_{\widetilde{\chi}_1^0} - \frac{0.011}{0.06 + (1 - \tau_{\widetilde{\chi}_1^0})^2}, \quad (9)$$

where $\tau_{\widetilde{\chi}_1^0}$ is in ns. This simple parameterization well characterizes the acceptance for any GMSB model to better than 4% and gives us confidence that it can be of use to future model builders.

Figure 23 shows the expected and observed cross section limits along with the NLO production cross section as a function of $\widetilde{\chi}_1^0$ lifetime at a mass of 100 GeV/c^2 and as a function of $\widetilde{\chi}_1^0$ mass at a lifetime of 5 ns, close to the limit of the expected sensitivity. Indicated is the 6.5% uncertainty-band on the production cross section. The band also shows the $\pm 1\sigma$ statistical variations of the expected cross section limit. Figure 24 shows the contours of constant 95% C.L. cross section upper limit based on the two observed data events and has its best sensitivity for lifetimes of ~ 5 ns. Figure 25 shows the 95% C.L. exclusion region for $\sigma_{\rm prod} > \sigma_{95}^{\rm exp}$ and $\sigma_{\rm prod} > \sigma_{95}^{\rm obs}$. Since the number of observed events is above expectations, $\sigma_{95}^{\rm obs}$ is slightly larger than $\sigma_{95}^{\rm exp}$. The $\widetilde{\chi}_1^0$ mass reach, based on the expected (observed) number of events, is 108 GeV/c^2 (101 GeV/c^2) at a lifetime of 5 ns. There is no exclusion of GMSB models with $\widetilde{\chi}_1^0$ lifetimes less than ~ 1 ns as only few of the $\widetilde{\chi}_1^0$ have a long enough lifetime to produce delayed photons. However, most of the parameter space

Requirement	Expected Background				Expected Signal	Data
	SM	Beam Halo	Cosmics	Total		
Photon, $\not{E}_T$, jet pre-selection cuts and						
$1.2 \leq t_{corr} \leq 10$ ns	490.74±295.40	0.27±0.12	1.30±0.49	492.3±295.4	11.7±1.4	398
$\not{E}_T > 40$ GeV	162.96±76.19	0.24±0.12	1.17±0.46	164.4±76.2	10.2±1.2	99
Jet $E_T > 35$ GeV	154.52±72.96	0.12±0.08	0.79±0.37	155.4±73.0	9.4±1.1	97
$\Delta\phi(\not{E}_T, \text{jet}) > 1.0$	13.07±11.57	0.10±0.07	0.52±0.30	13.7±11.6	8.5±1.0	8
$2 \leq t_{corr} \leq 10$ ns	0.71±0.60	0.07±0.05	0.46±0.26	1.3±0.7	5.7±0.7	2

TABLE XII: Summary of the expected and observed number of events from the background estimate after the preselection sample requirements and each requirement from the optimization, separated for each background, and the expected number of signal events. The expected signal numbers are for a GMSB example point at $m_{\tilde{\chi}_1^0} = 100$ GeV/c^2 and $\tau_{\tilde{\chi}_1^0} = 5$ ns. Note that the additional requirement $1.2 < t_{corr} < 10$ ns is applied at the top line to allow the background estimation methods to use the prompt control region to make predictions at each stage. The preselection sample cuts are listed in Table V. The background predictions match well with the observed number of events for each requirement indicating the background estimation methods are reliable. There is no evidence of new physics.
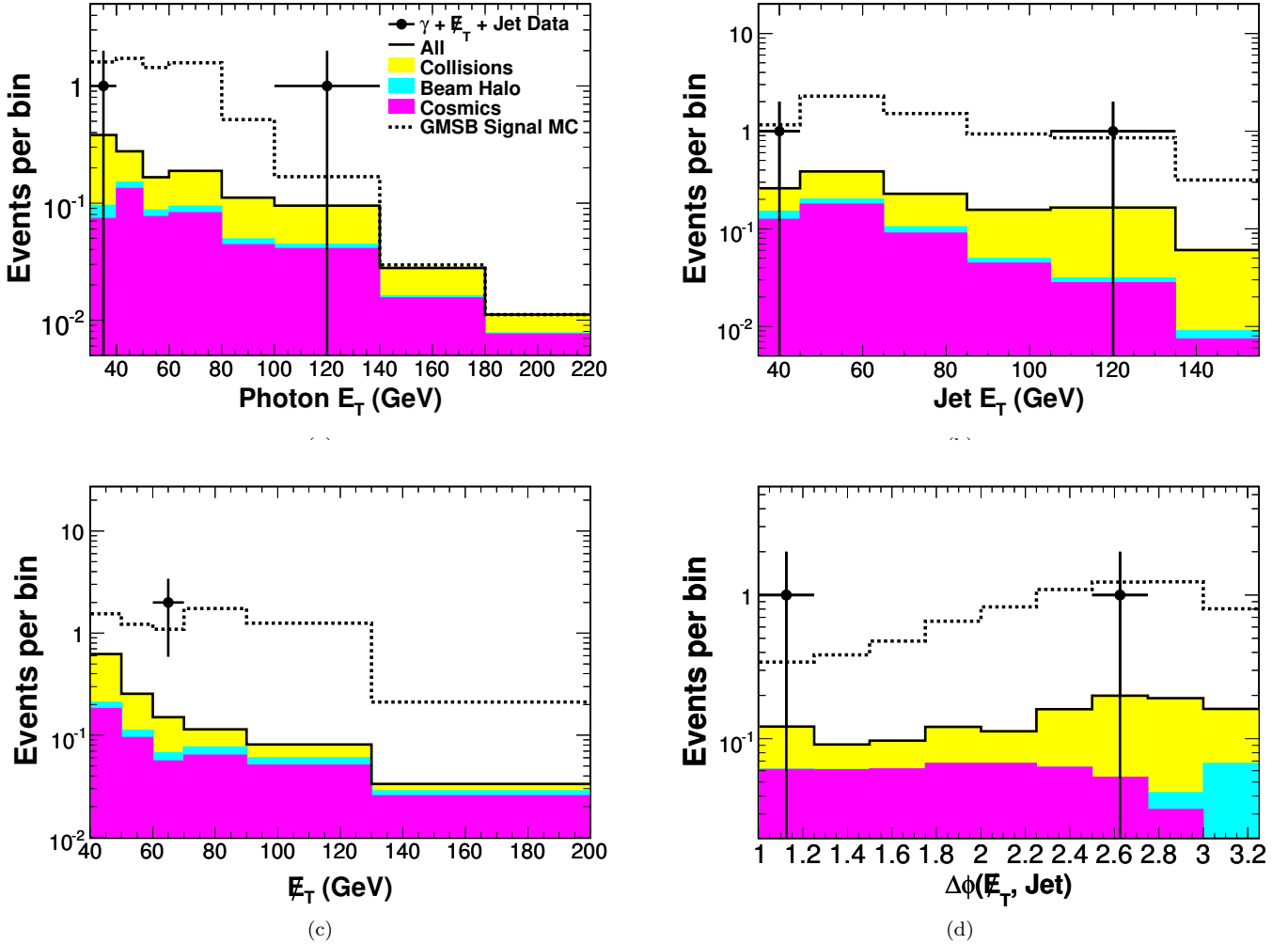

FIG. 22: The predicted and observed photon E_T, jet E_T, $\not{E}_T$, and $\Delta\phi(\not{E}_T, \text{jet})$ distributions for the signal region after the final event selection requirements. The GMSB distributions are for $m_{\tilde{\chi}_1^0} = 100$ GeV/c^2 and $\tau_{\tilde{\chi}_1^0} = 5$ ns. There is no evidence for new physics.
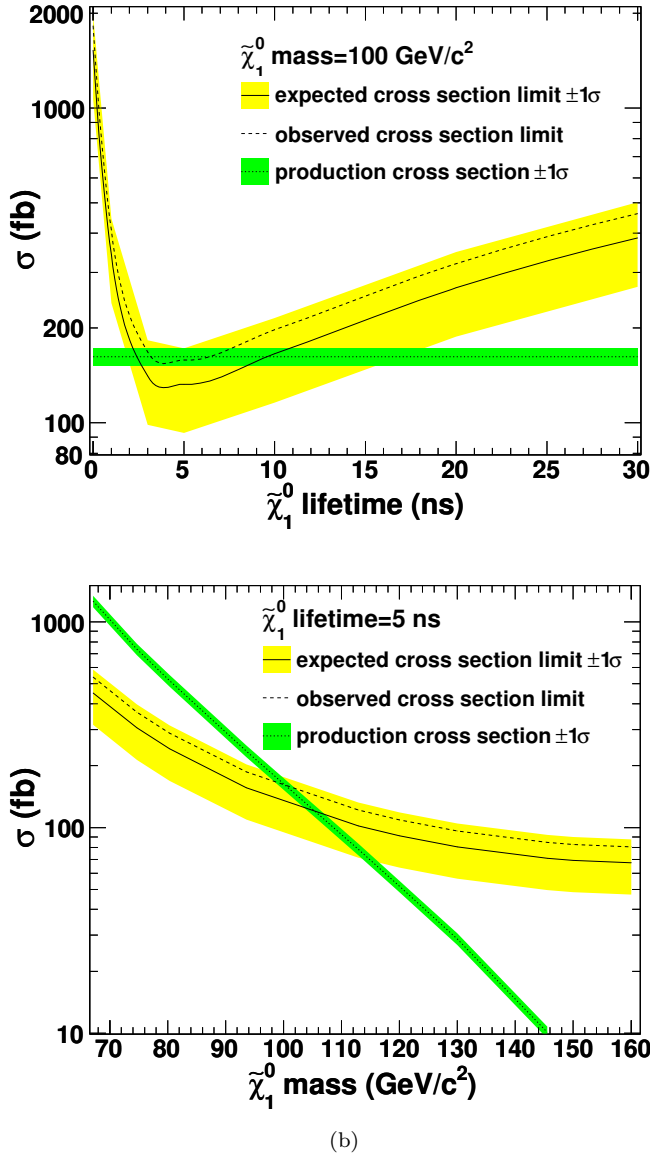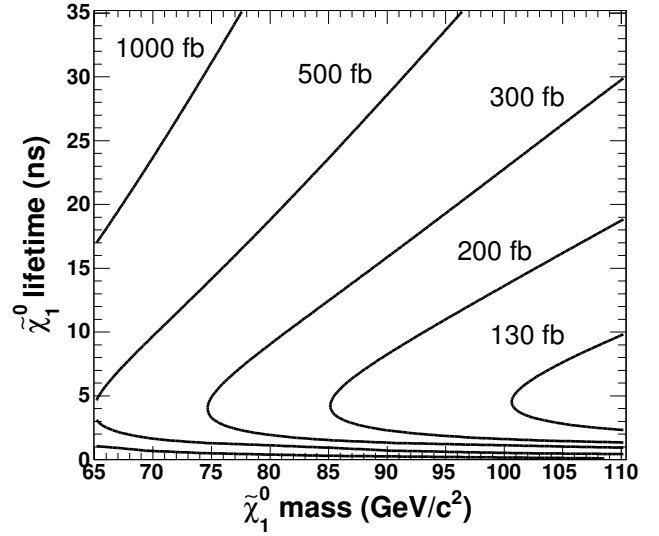
FIG. 24: The contours of constant 95% C.L. cross section upper limit for the observed number of events in the detector.

(b)

FIG. 23: The expected and observed cross section limits as a function of the $\widetilde{\chi}_1^0$ lifetime at a mass of 100 GeV/c^2 (a) and as a function of the $\widetilde{\chi}_1^0$ mass at a lifetime of 5 ns (b). Shaded green (darker shading) is the 6.5% uncertainty-band for the production cross section. The yellow shaded region (lighter shading) is the variation in the expected limit due to the statistical variation on the number of background events in the signal region ($\sim$30%).

there is already excluded by searches in $\gamma\gamma + \not{E}_T$ [9, 10]. The large mass limits extend beyond those of the LEP searches [10] (using photon "pointing" methods) and are currently the world's best.

B.   Future Prospects

This search extends the exclusion region close to the most important region of GMSB parameter space where the $\widetilde{G}$ is predicted to be thermally produced in the early
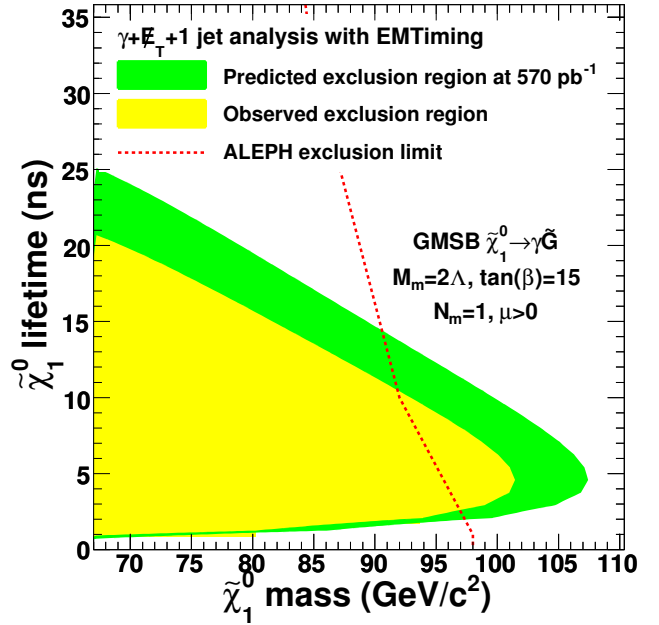

FIG. 25: The expected and observed 95% C.L. exclusion region along with the most stringent published LEP limits from ALEPH [10]. The highest mass reach of 108 GeV/c^2 (expected) and 101 GeV/c^2 (observed) is achieved at a lifetime of 5 ns.

universe with a mass of 1-1.5 keV/c^2 [13]. With a higher luminosity this search technique will be sensitive to this mass range. To investigate the prospects of such a search we calculate the expected cross section limit assuming, for simplicity, that all backgrounds scale linearly with luminosity (the uncertainties remain a constant fraction of the background). While this assumption allows for

a quick estimate, it does not reflect the probable improvements in the background rejection methods or the worsening effects due to the higher instantaneous luminosity that could cause a higher fraction of background events with a wrong-vertex selection. As these effects would tend to balance each other, it can be considered to provide a reasonably balanced estimate. The resulting cross section limit improvement, along with the expected 95% C.L event limit, N_{95}^{exp}, are shown in Table XIII for our example point at $m_{\widetilde{\chi}_1^0} = 100$ GeV/c^2 and $\tau_{\widetilde{\chi}_1^0} = 5$ ns. Figure 26 shows the expected exclusion region for a luminosity of 2 and 10 fb^{-1} along with the parameter space where $1 \leq m_{\widetilde{G}} \leq 1.5$ keV/c^2. The figure suggests that this search technique will be sensitive to all of this important parameter space at 10 fb^{-1} luminosity for $\widetilde{\chi}_1^0$ masses of less than $\sim$140 GeV/c^2 and lifetimes of less than 30 ns.

Luminosity (fb^{-1})	Expected Background	Factor of Improvement on σ_{exp}	N_{95}^{exp}
0.570	1.3±0.7 (2)	1	4.6 (5.5)
2	4.3±2.3	0.46	7.4
10	21.9±11.6	0.0308	24.8

TABLE XIII: The expected search sensitivity improvement for various luminosities for a GMSB example point at $m_{\widetilde{\chi}_1^0} = 100$ GeV/c^2 and $\tau_{\widetilde{\chi}_1^0} = 5$ ns assuming all backgrounds and their uncertainty fractions scale linearly with luminosity. The numbers in parentheses reflect the observed values in this search. The resulting exclusion region is shown in Fig. 26.
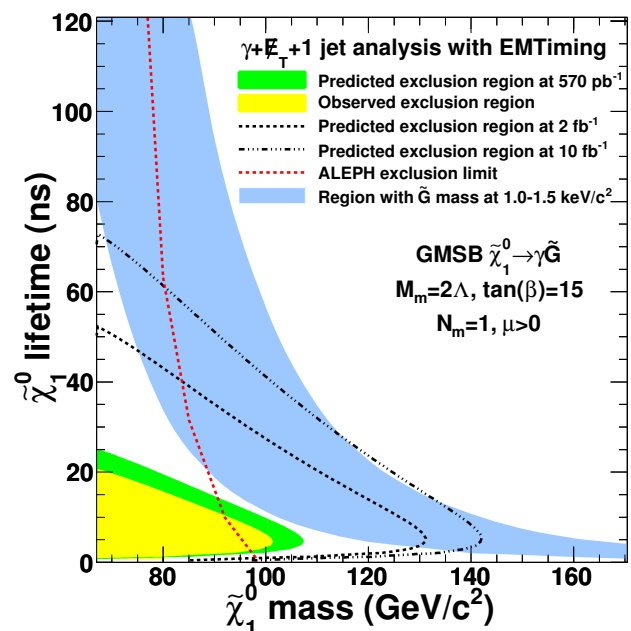
VIII. CONCLUSION

We have presented a search for heavy, long-lived neutralinos that decay via $\gamma\widetilde{G}$ in a sample of $\gamma + \mathrm{jet} + \not{E}_T$ events from $p\bar{p}$ collisions at $\sqrt{s} = 1.96$ TeV using the CDF II detector. Candidate events were primarily selected based on the delayed arrival time of the photon at the calorimeter as measured with the newly installed EMTiming system. In 570 pb^{-1} of data collected during 2004-2005 at the Fermilab Tevatron, two events were observed, consistent with the background estimate of 1.3±0.7 events. As the search strategy does not rely on event properties specific to GMSB models, any delayed $\gamma + \mathrm{jet} + \not{E}_T$ signal (that passes our kinematic sample cuts) is excluded at 95 % C.L if it produces more than 5.5 events. This result allows for setting both quasi model-independent cross section limits and for an exclusion region of GMSB models in the $\widetilde{\chi}_1^0$ lifetime vs. mass plane, with a mass reach of 101 GeV/c^2 at $\tau_{\widetilde{\chi}_1^0} = 5$ ns. These results extend the sensitivity to these models beyond those from LEP II [10] and are the world's best at masses > 90 GeV/c^2. By the end of Run II, an integrated luminosity on the order of 10 fb^{-1} might be collected, for which we estimate a mass reach of $\simeq 140$ GeV/c^2 at a lifetime of 5 ns by scaling the expected number of background events.

FIG. 26: The expected 95% C.L. exclusion region after a scaling of the background prediction and the uncertainties for a luminosity of 2 fb^{-1} and 10 fb^{-1} respectively. The shaded band shows the parameter space where $1 \leq m_{\widetilde{G}} \leq 1.5$ keV/c^2.

Photon and Electron Identification Variables	
Ficucial	$|X_{\text{CES}}| < 21$ cm and $9 < |Z_{\text{CES}}| < 230$ cm for the calorimeter cluster centroid
$E_{\text{Had}}/E_{\text{EM}}$	The ratio of the energy deposited in the hadronic calorimeter behind the cluster to the energy in the cluster as measured in the EM calorimeter
E^{Iso} (GeV)	Energy in a cone of $\Delta R = \sqrt{\Delta\phi^2 + \Delta\eta^2} = 0.4$ around the object, excluding the cluster energy
Ntracks	Number of tracks pointing at photon cluster
Σp_T (GeV/c)	Total p_T of tracks in a cone of $\Delta R = 0.4$ around the cluster
$E^{2^{\text{nd}}\text{cluster}}$ (GeV)	Energy of a second EM cluster, if any, as identified in the shower-maximum detector
A_P	$\frac{|E_{\text{PMT1}} - E_{\text{PMT2}}|}{E_{\text{PMT1}} + E_{\text{PMT2}}}$ where E_{PMT1} and E_{PMT2} are the two PMT energies
E/p	Ratio of the electron energy as measured in the calorimeter to the momentum as measured by the COT
χ^2_{Strip}	A χ^2 comparison of the shower-maximum profile to test beam data expectations
$Lshr$	A comparison of the energy deposition of the electron, in adjacent towers, to expectations
$\Delta x \cdot q$ (cm)	The comparison between the extrapolated track position into the shower-maximum detector and the measured cluster centroid position, taking into account the track charge
z_0 (cm)	The measured z position of the electron track along the beam line
Δz (cm)	Difference between the measured electron track z_0 and the measured z_0 of the vertex
Good Track Selection Variables	
Slow Proton rejection	The dE/dx for the track as it traverses the COT is not consistent with being from a slow proton. We require the timing variable to be less than 20 ns. For a description of the relationship between the timing measurement and dE/dx see [21].
z_0 (cm)	The measured z position of the track along the beam line
$\text{Err}(z_0)$ (cm)	Uncertainty on the z_0 measurement
t_0 (ns)	The measured time of the track origin
$\text{Err}(t_0)$ (ns)	Uncertainty on the t_0 measurement

TABLE XIV: A description of the identification variables used in this analysis for electrons, photons, and tracks.

Appendix: ID Variables

In Table XIV we provide a description of the identification variables used in this analysis for electrons, photons, and tracks.

REFERENCES

proton beam, θ as the polar angle, ϕ as the azimuthal angle relative to the horizontal plane and $\eta = -\ln\tan(\theta/2)$. We take $E_T = E\sin\theta$ and $p_T = p\sin\theta$ where E is the energy measured by the calorimeter and p the momentum measured in the tracking system. If no vertex is reconstructed we use $z_{\text{collision}} = 0$. We define $\vec{\not{E}}_T = -\sum_i E_T^i \vec{n}_i$ where $\vec{n}_i$ is a unit vector in the transverse plane that points from the interaction vertex to the ith calorimeter tower. $\not{E}_T$ is the magnitude of $\vec{\not{E}}_T$.

[1] M. Dine, and A. Nelson, Phys. Rev. D **48**, 1277 (1993); S. Ambrosanio *et al.*, Phys. Rev. D **54**, 5395 (1996); C. Chen and J. Gunion, Phys. Rev. D **58**, 075005 (1998).

[2] S. Martin, arXiv:hep-ph/9709356.

[3] P. Bode, J. Ostriker and N. Turok, Astrophys. J. 556, 93 (2001).

[4] F. Abe *et al.* (CDF Collaboration), Phys. Rev. Lett. **81**, 1791 (1998) and Phys. Rev. D **59**, 092002 (1999).

[5] In this paper we assume a cylindrical coordinate system that defines z as the longitudinal axis along the

[6] J. Feng, S. Su, and F. Takayama, Phys. Rev. D **70**, 075019 (2004), and references therein.

[7] A. Abdulencia *et al.* (CDF Collaboration), Phys. Rev. Lett. **99**, 121801 (2007); P. Wagner, Ph.D. Thesis, Texas A&M University, FERMILAB-THESIS-2007-14.

[8] T. Aaltonen *et al.* (CDF Collaboration), arXiv:hep-ex/0708.3642v1, accepted for publication in Phys. Rev. D.

[9] D. Acosta *et al.* (CDF Collaboration), Phys. Rev. D **71**, 031104 (2005). V. Abazov *et al.* (D0 Collaboration), Phys. Rev. Lett. **94**, 041801 (2005).

[10] A. Heister *et al.* (ALEPH Collaboration), Eur. Phys. J. C **25**, 339 (2002); also see M. Gataullin *et al.*, for the L3 Collaboration, arXiv:hep-ex/0611010; G. Abbiendi *et al.* (OPAL Collaboration), Proc. Sci. HEP2005 346 (2006); J. Abdallah *et al.* (DELPHI Collaboration), Eur. Phys. J. C **38** 395 (2005).

[11] J. L. Feng and T. Moroi, Phys. Rev. D **58**, 035001 (1998).

[12] B. Allanach *et al.*, Eur. Phys. J. C **25**, 113 (2002).

[13] E. Baltz *et al.*, J. High Energy Phys. **0305**, 067 (2003).

[14] P. Wagner and D. Toback, Phys. Rev. D **70**, 114032 (2004).

[15] For a description of how clusters of energy, for example $\tau^{\pm} \to \pi^{\pm}\pi^{\mp}\pi^{\pm}\nu_{\tau}$ decays, are identified as jets, see F. Abe *et al.* (CDF Collaboration), Phys. Rev. Lett. **68**, 1104 (1992). For a discussion of the jet energy measurements, see T. Affolder *et al.* (CDF Collaboration), Phys. Rev. D **64**, 032001 (2001). For a discussion of standard jet correction systematics, see A. Bhatti *et al.*, Nucl. Instrum. Methods, A 566, 375 (2006). We use jets with cone size $\Delta R = 0.7$.

[16] M. Goncharov *et al.*, Nucl. Instrum. Methods Phys. Res., Sect. A **565**, 543 (2006).

[17] Y. Liu, Ph.D. Thesis, Université de Genève, FERMILAB-THESIS-2004-37.

[18] T. Sjöstrand *et al.*, Comput. Phys. Commun. **135**, 238 (2001). We use version 6.216.

[19] The incident angle α variation is due to the vertex position z_0 variation. The calorimeter towers point to the center of the detector, so the angle extends out to $\sim 18° \approx \arctan(\frac{60 \text{ cm}}{183 \text{ cm}})$, where 60 cm is the maximal z_0 variation and 183 cm is the radius from the beamline to the photon shower maximum in the detector.

[20] R. Brun *et al.*, CERN-DD/EE/84-1 (1987). The EM-Timing system is done separately as a parametrized simulation.

[21] D. Tonelli, Ph.D. Thesis, Scuola Normale Superiore, Pisa, FERMILAB-THESIS-2006-23.

[22] D. Acosta *et al.* (CDF Collaboration), Phys. Rev. D **71**, 052003 (2005).

[23] Note that throughout this section a "vertex" refers to the true underlying collision, whereas the term "cluster" refers to the clustered set of tracks that constitute the reconstructed vertex.

[24] G. McLachlan and D. Peel, Wiley-Interscience, ISBN 0471006262.

[25] D. Acosta *et al.* (CDF Collaboration), Phys. Rev. Lett. **89**, 281801 (2002).

[26] We note that this occurs in $\sim 14\%$ of the cases for this sample. While this is an interesting number, the fraction of events where the wrong vertex is picked is very sample dependent as it depends only on the probability that the highest-Σp_T vertex in the event is the same vertex that produces the photon. For the luminosity for the data taking period there are, on average, between 0.4 and 4.4 min-bias collisions per event. As a comparison SM $Z\gamma \to \nu\nu\gamma$ production produces very few tracks in association with the photon so there is a lower probability that the highest-Σp_T vertex produces the photon at high luminosity. As a second example, in $t\bar{t}\gamma \to \gamma + \text{jets}$ events the photon is very likely to come from the highest-Σp_T vertex.

[27] F. Paige and S. Protopopescu, BNL Report BNL38034, 1986; F. Paige, S. Protopopescu, H. Baer and X. Tata, hep-ph/0001086. We used version 7.64 to generate the SUSY masses.

[28] A. Abulencia *et al.* (CDF Collaboration), J. Phys. G. **34**, 2457 (2007); J. Pumplin *et al.*, J. High Energy Phys. **0207**, 012 (2002); J. Huston *et al.*, J. High Energy Phys. **0310**, 046 (2003).

[29] P. Simeon and D. Toback, J. of Undergrad. Research in Phys. **20**, (2007).

[30] Multiple collisions in the event can produce extra vertices, one of which can be picked incorrectly as the event vertex and cause t_{corr} to be systematically mismeasured. To take this effect into account in the acceptance calculation, an extra vertex is simulated for each event with a z_0 and t_0 that are randomly selected from Gaussians with $\sigma_z = 30$ cm and $\sigma_t = 1.3$ ns. To estimate the impact on the acceptance from a variation of the wrong-vertex fraction depending on the event requirements, the wrong-vertex fraction is varied between 0% and 10%, obtaining an acceptance variation of $< 1.5\%$.

[31] See W. Beenakker *et al.*, Nucl. Phys. B **492**, 51 (1997); We use PROSPINO2.0.

[32] J. Conway, CERN Yellow Book Report No. CERN 2000-005 (2000), p. 247.

[33] E. Boos, A. Vologdin, D. Toback and J. Gaspard, Phys. Rev. D **66**, 013011 (2002).

[34] W. Beenakker *et al.*, Phys. Rev. Lett. **83**, 3780 (1999).

[35] J. L. Feng, A. Rajaraman and F. Takayama, Phys. Rev. D **68**, 063504 (2003); M. J. Strassler and K. M. Zurek, arXiv:hep-ph/0605193.